Title: Systematic Evaluation of the Influence of Camera Placement and Settings on the Quality of Photogrammetric Models of Rocks

Authors: Alex P. Clarke[1*], Richard Haas[1], Friedrich Hawemann[1], Virginia Gail Toy[1,2]

Affiliations:

1. Institut für Geowissenschaften, Johannes Gutenberg-Universität Mainz, J. J. Becher-Weg 21, D-55128, Mainz, Germany
2. Department of Geology, University of Otago, P.O. Box 56, Dunedin 9054, New Zealand

Corresponding Author:

Dr. Alex P. Clarke, alex.clarke@uni-mainz.de

Acknowledgements:

A.P. Clarke was funded by the Alexander von Humboldt Foundation. This article was prepared from the thesis of Mr. Richard Haas, a masters student at Johannes Gutenberg-University Mainz.

Systematic Evaluation of the Influence of Camera Placement and Settings on the Quality of Photogrammetric Models of Rocks

Clarke, A.P.[1], *Haas, R.*[1], *Hawemann, F.*[1], *Toy, V.G.*[1,2]

1. Institut für Geowissenschaften, Johannes Gutenberg-Universität Mainz, J. J. Becher-Weg 21, D-55128, Mainz, Germany
2. Department of Geology, University of Otago, P.O. Box 56, Dunedin 9054, New Zealand

Email: alex.clarke@uni-mainz.de

Abstract

Despite the widespread adoption of photogrammetry across diverse disciplines, the relative influences of image acquisition parameters on the quality of photogrammetric models are seldom quantitatively understood. To address this, we conducted experiments under controlled lighting conditions, camera positions, and camera settings and evaluated the quality of the resultant models using both a subjective rating and a quantitative comparison. In total, 2541 models were evaluated in this study. In general, higher quality models can be produced by minimising large changes in the direction of view between adjacent images. Strong digital noise due to high ISO is detrimental to model quality, although this may be partially mitigated by noise reduction post-processing. RAW images generally produce higher quality models than JPEG images; however, at high ISOs, RAW images may result in poorer quality models due to their inherent lack of pre-applied noise reduction. Images taken with a smartphone produced models of comparable quality to those taken with a dedicated camera. Models were not consistently reproducible, even with near-identical images; therefore, practitioners must be aware of their margins of error when interpreting photogrammetric results. This study therefore provides practical guidance for practitioners based on a robust parameter study using natural geological samples.

Graphical Abstract

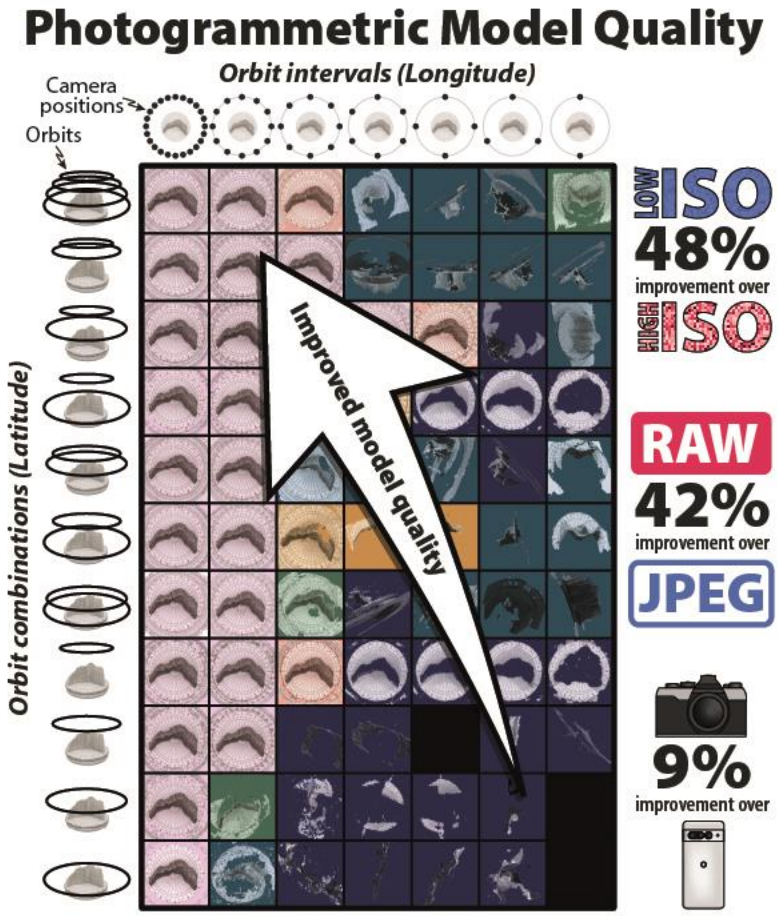

Keywords: Photogrammetry; Model quality; Camera placement; Camera settings; Evidence-based guidance.

1. Introduction

The use of photogrammetry has increased significantly in recent years (Marín-Buzón *et al.* 2021; Polidori 2021) — especially in geosciences where it is routinely used to create virtual outcrop models (Cawood *et al.* 2017; Howell *et al.* 2021; Pugsley *et al.* 2022) and archaeology where models record both artefacts and sites (Williams *et al.* 2019; Kanun *et al.* 2021; Bisson-Larrivée and LeMoine 2022) — and yet the relative influence of factors affecting the quality of photogrammetric models is seldom understood by practitioners (Dall'Asta *et al.* 2015; O'Connor 2018). Practical considerations such as acquisition time, availability of light, and accessibility of viewpoints typically limit the placement and settings of cameras (Cawood *et al.* 2017; Burdziakowski and Bobkowska 2021). In this study, we evaluate the influence of common variables — camera placement, ISO, image format (JPEG [Joint Photographic Experts Group] and RAW), and camera selection — on the quality of resulting photogrammetric models to assist the practitioner in addressing the priorities of their photogrammetric survey.

The overall "quality" of a photogrammetric model is generally understood to refer to the scale of observable detail relative to the scale of the model, the geometric accuracy of reconstructed objects, and the completeness of the model (Luhmann *et al.* 2023). Additionally, for geospatial applications, the accuracy of the location and orientation of the model to an external reference frame also contributes to the quality of the model (Historic England 2017; Barba *et al.* 2019). The geospatial accuracy of photogrammetric models is often assessed and quantified by comparison against external reference data, such as LiDAR scans, GPS/GNSS measurements of ground control points (GCPs), and compass measurements (Cawood *et al.* 2017; Oniga *et al.* 2018; Barba *et al.* 2019; Fawzy 2019).

Camera networks — the arrangement and orientations of camera positions in a photogrammetric survey (Fig. 1) — may either be designed with a regular arrangement of cameras irrespective of the geometry of the subject or the placement of cameras may be adapted to ensure all parts of the subject are optimally imaged (Smith *et al.* 2018; Li *et al.* 2023); however, in practice, cameras are typically placed non-systematically, often strongly influenced by the available viewpoints from which to image the subject (Cawood *et al.* 2017). Cameras may be arranged such that their optic axes are aligned (as is common in aerial surveys [James *et al.* 2017; Gargari *et al.* 2023]), converge in the direction of view (such as for turntable studies [Tannus 2020; Cunningham 2021; Wang and Jaw 2021; Fawzy *et al.* 2024, Yiğit *et al.* 2025]), or diverge in the direction of view (for instance, in interior photogrammetry [Georgantas *et al.* 2012; Ziegler and Loew 2019; Cazes *et al.* 2025]). As every part of the object must be imaged at least twice from different camera positions, an overlap between the fields of view of adjacent images greater than 50% is necessary to prevent gaps in the resultant model, with most guidance recommending between 60% and 70% for ideal camera networks (Fig. 1D) (Waldhäusl and Ogleby 1994a, b; Historic England 2017; Guidi *et al.* 2020; Cunningham 2021). However, overlap may not be relevant when camera optic axes are strongly convergent as the same point may be seen in all images but have undergone radical distortions from the perspective of the camera (Yu and Morel 2011; Wang *et al.* 2025). It is also generally well-established that the quality of photogrammetric results scales with the number of images used, although at the cost of additional acquisition and processing time (Barba *et al.* 2019; Cunningham 2021). However, the inclusion of images from suboptimal camera positions may degrade precision and introduce noise which is detrimental to model quality (Barba *et al.* 2019).

The level of detail reconstructed in a photogrammetric model depends strongly on the level of detail visible in the input imagery which, in turn, is determined by the resolution of the camera sensor, the optics and settings of the camera and lens system, and the working distance between the camera and the subject surface (Fig 1A) (Historic England 2017; Luhmann *et al.* 2023). The camera resolution, sensor size, focal length and the working distance may be considered together as the *Ground Sampling Distance* (GSD); a metric which measures the distance in real space between the centres of the areas represented by each pixel on the camera sensor (Fig 1A & B) (Reulke and Eckardt 2013; Luhmann *et al.* 2023). However, for subjects with non-planar geometry — the primary targets of photogrammetric reconstruction — or when images are taken at an oblique angle to the surface, GSD can vary wildly, even within a single photograph (Fig 1C) (Guidi *et al.* 2020). Additionally, GSD does not consider optical effects, such as blur or aberrations, which influence the perceivable detail in an image; this is especially relevant to the physically small but high-resolution sensors on many consumer cameras and smartphones where the perceivable detail is limited by the diffraction blur spot (Airy disk) size, meaning that they may resolve less detail than larger but lower (pixel-) resolution sensors (Fig 1F) (Tisse *et al.* 2008; Historic England 2017; Tóth 2017; Patonis 2024). GSD also refers only to the input imagery and not to the resultant model, the quality of which is strongly influenced by the settings used in the photogrammetric process. Despite the drawbacks of GSD in determining the quality of a photogrammetric model, the general principle holds that — all else being equal — photogrammetric quality can be improved by the use of closer working distances and/or higher resolution sensors (Guidi *et al.* 2020).

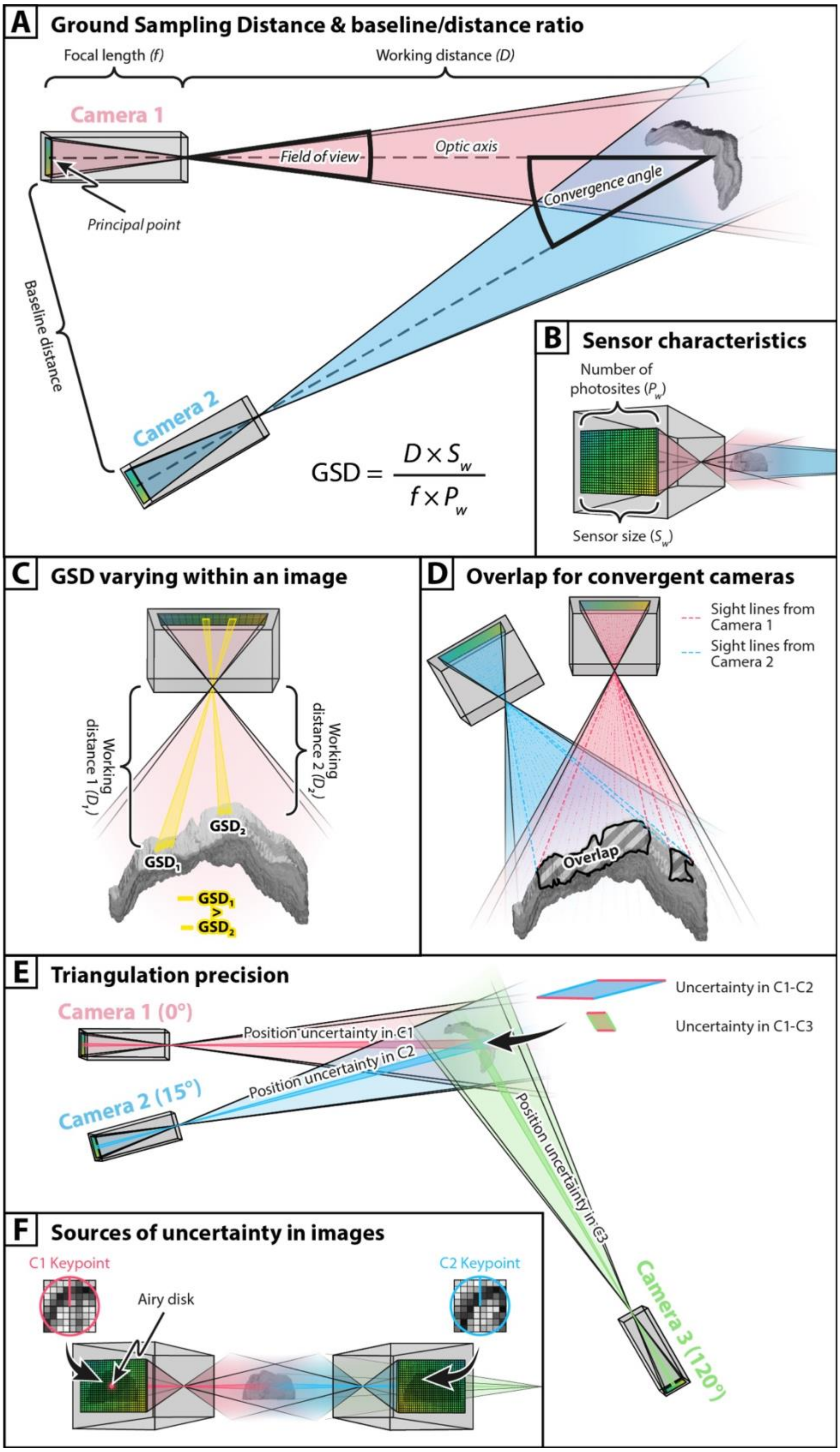

Figure 1: Key concepts in photogrammetric survey design. A) Parameters and equation to calculate Ground Sampling Distance (GSD) and baseline to distance ratio. B) Sensor characteristics for the calculation of GSD. C) Demonstration that the varying working distances

between the camera and an irregular object result in varying GSD values within a single image. D) Overlap for convergent cameras showing the region within shared line-of-sight from both cameras. E) Demonstration of triangulation precision showing exaggerated regions of uncertainty. The region of combined triangulation uncertainty for the camera pair with a 120° offset is markedly smaller than the uncertainty region for the camera pair with 15° offset, meaning that the 120° camera pair is more precise. F) Sources of uncertainty in images showing an Airy disk larger than photosites and matched keypoints with a sub-pixel offset.

In addition to the working distance, the distance from one camera to a neighbouring camera — referred to as the *baseline* distance — is known to influence the triangulation precision of points on the reconstructed surface, with larger baseline/distance ratios improving precision, especially of depth estimates (Fig 1E) (Hottier 1976; Fraser 1984; Olson and Abi-Rached 2010; Hahne *et al.* 2018; Guidi *et al.* 2020). Baseline/distance ratios of 1:1 – 1:15 are typically recommended (Waldhäusl and Ogleby 1994a, b) — equating to an angular difference of 60° – 4° respectively in the case of convergent cameras — and Fraser (1984) noted that angular differences of 120° resulted in the theoretical minimum of triangulation error. However, it has also long been noted that automated feature detection and matching algorithms integral to modern photogrammetry can struggle to make correct associations between image pairs if the perspective change between images is too great (Olson and Abi-Rached 2010; Guidi *et al.* 2020). As such, camera network design involves a compromise between triangulation accuracy which improves with wider baseline distances and point matching accuracy which improves — in the case of convergent cameras — with more similar perspectives which result from narrow baseline distances (Guidi *et al.* 2020).

Modern computational photogrammetry relies on the identification, description, and matching of distinctive features between images (Huang *et al.* 2024). This is accomplished through the use of feature descriptors which provide a numerical representation (usually as a high-dimensional vector) of the pixels within distinctive patches — usually a few tens of pixels in size — of the image, referred to as *keypoints* (Fig 1F) (Lowe 1999, 2004; Rublee *et al.* 2011). These keypoints are then compared between images to find the closest match between these numerical representations. As such, an exact match between feature descriptors is not needed to make correct associations and feature descriptors may be tolerant to changes in illumination, digital noise, artefacts, or small changes in the shape of the feature (Li *et al.* 2017). Different feature descriptors may be invariant to different kinds of distortion in the image. For instance, SIFT (Scale Invariant Feature Transform, Lowe 2004) — a popular example of a feature descriptor — is invariant to isotropic scaling and rotation but not to anisotropic scaling, skews, or perspective distortions (Yu and Morel 2011; Wang *et al.* 2025).

The image quality of each input image strongly influences the quality achievable by photogrammetry (Sieberth 2020). The pixel resolution and scale of observable detail, presence of motion and optical blur in the image, the amount of digital noise, and the format the image is recorded in all influence the image quality. The maximum resolution (in pixels) of an image produced by a digital camera is determined by the number of photosites present on the camera sensor. As a pixel is the smallest unit of detail in a digital image, an increased number of pixels allows for the recording of a more detailed image. However, diffraction at the aperture prevents focussing of light to a point and instead creates a spot of finite size on the sensor, known as the Airy disk, which also imparts a physical limit on the resolvable detail; this effect is stronger as the Airy disk becomes larger at smaller apertures (Luhmann *et al.* 2023). Small sensors such as those in smartphones and Micro-Four-Thirds cameras often feature photosites that are several times smaller than the Airy disk and so often resolve less detail than physically larger but lower resolution sensors (Tisse *et al.* 2008; Historic England 2017; Tóth 2017; Patonis 2024).

Motion blur may arise from either the camera moving, the subject moving, or both (Sieberth *et al.* 2014b). The degree of motion blur may vary throughout the image depending on the motion in the scene, the distance from the camera, and the parallax effect (Torres and Kämäräinen 2023). In settings where motion cannot be eliminated, faster shutter speeds may limit motion blur at the cost of light on the camera sensor (Howell *et al.* 2021). Optical image stabilisation — which attempts to compensate for camera motion by shifting the sensor and/or lens elements — is often effective at reducing motion blur due to camera shake; however, this alters the *intrinsic* parameters (namely the *principal point* where the optic axis of the camera intersects with the image plane) of the camera system in a manner which cannot be recovered, potentially negatively influencing photogrammetric reconstruction (Historic England 2017). Optical blur increases from the plane of sharp focus, with the distance in front of and behind this plane in which the image is acceptably sharp defined as the *depth of field*. As such, the amount of optical blur in an image varies throughout the frame (Pan 2019). The depth of field may be increased through the use of a smaller aperture, albeit at the cost of light on the camera sensor and an increased Airy disk size (Tóth 2017). This compromise can be avoided, however, through the use of focus stacking, where multiple exposures of the same scene taken at different focal distances are composited into a single sharp image (Kontogianni *et al.* 2017; Olkowicz *et al.* 2019), although this can also introduce artefacts and distortions (Faure *et al.* 2025). Both optical and motion blur are well known to degrade the quality of photogrammetric models (Sieberth *et al.* 2014b, a; Pan 2019; Sieberth 2020); however, the difference-of-gaussians process involved in many modern feature matching algorithms does allow feature points to be correctly matched despite the presence of blur, providing that their shape can still be discerned (Lowe 1999). In addition to blur, the amount of digital noise in a scene also degrades image quality and may confound feature matching algorithms by changing the shape of identified features (O'Connor 2018). Digital noise is inherent to any digital photograph but may become apparent due to the amplification at high ISOs of a weak signal in cases of poor lighting (Healey and Kondepudy 1994). Modern noise reduction algorithms are often very effective at removing digital noise but the detail lost in a noisy image cannot be recovered (Plötz and Roth 2017; Elad *et al.* 2023).

Additionally, the format the images are recorded in also influences the quality of images and photogrammetric models. Many dedicated cameras can save images as either RAW files — containing the basic information captured by the sensor at the maximum bit-depth and without post-processing or compression — or JPEG files which are compressed and have in-camera image edits permanently applied (Alfio *et al.* 2020). Many smartphones and consumer cameras only allow recording of images as JPEG. JPEG compression artefacts are often visible around high-contrast edges and have been shown by several studies to interfere with feature matching in the photogrammetric process (e.g., Akçay *et al.* 2017; Alfio *et al.* 2020; Małyszek and Mitka 2024).

Rocks are common subjects for photogrammetric studies, not just in the field of geoscience (e.g., Bilmes *et al.* 2019; Howell *et al.* 2021; Buckley *et al.* 2022) but also in archaeology and cultural heritage (Bryan and Clowes 1997; Kanun *et al.* 2021; Hodač *et al.* 2023; Sorrentino *et al.* 2023), and urban surveying (Deliry and Avdan 2021; Garilli *et al.* 2021) where artefacts or buildings are commonly made of stone. These materials are generally opaque and have a matt lustre and a feature-rich non-repeating texture which is well-suited to photogrammetric reconstruction (Nielsen *et al.* 2022; Surmen 2023), although they may be polished or contain crystals which are transparent and/or specular reflectors. However, both natural and worked rocks often have complex and irregular geometries which require care to fully image and to ensure correct focus (Cawood *et al.* 2017; Surmen 2023; Faure *et al.* 2025). Within geoscience, photogrammetric virtual outcrop models are frequently used to extract the orientation and position of discontinuities such as fractures, joints, bedding, and faults for structural analysis (e.g., Bemis *et al.* 2014; Lund Snee *et al.* 2014; Bonato *et al.* 2022; Cawood *et al.* 2022; Panara *et al.* 2022; Uzkeda *et al.* 2022) or to demonstrate features for teaching purposes (e.g., Fleming 2022; Harknett *et al.* 2022; Rutkofske *et al.* 2022; Pugsley *et al.* 2024; Thomann *et al.* 2024). Photogrammetric models may also support ground motion and landscape evolution surveys (e.g., Eltner *et al.* 2017; Sun *et al.* 2024) and morphometric palaeontological studies (e.g., Novikov *et al.* 2019; Cunningham 2021; Lallensack *et al.* 2022), among other use cases.

In this study, we imaged rock samples under controlled lighting conditions, relative camera positions, and camera settings to isolate the influence of each of the studied factors on photogrammetric model quality. Namely, the variables of camera placement, ISO and digital noise, image format (JPEG or RAW), and camera choice (dedicated camera or smartphone camera) are here compared against each other. We evaluated model quality using both subjective and quantitative assessment of photogrammetric models and by modelling the connectedness of the camera network. This study shows that camera network design is the predominant control on photogrammetric model quality, with the best models arising from evenly-spaced camera networks with small changes in perspective between adjacent camera positions. The quality of models produced from images taken at ISO 200 was, on average, 48% better than models created from images taken at ISO 25600, use of RAW images improved model quality by an average of 42% compared to JPEG images, and the dedicated camera and smartphone produced models with nearly equal quality.

2. Methods

2.1. Image acquisition and model creation

To investigate the influences on photogrammetric reconstruction of geological materials, we selected three rock samples with varied shapes and surface features for this study (Fig. 2): a sideritic marble with a saccharoidal texture and siderite druses showing flanking folds (Passchier 2001) (length: 19 cm, breadth: 10 cm, height: 5 cm), a schist with parasitic folds at a range of scales (length: 16 cm, breadth: 6 cm, height: 6 cm), and a granite showing a striated fracture surface (length: 14 cm, breadth: 8.5 cm, height: 1 cm). The marble sample was selected as it displays surfaces both perpendicular and parallel to the turntable stage and these surfaces contain high relief topography and overhanging regions. The schist sample was selected as the dominant surface was oriented at a high angle to the turntable stage with only a thin edge oriented parallel to the stage. Additionally, the folds are self-similar across scales and serve as a useful indicator of the spatial resolution of the models, and the hinges of the folds mark deep grooves in the sample surface. The granite sample was selected because the majority of the sample surface is sub-parallel to the stage, there is high colour contrast between the white feldspar and the black biotite grains, and the shallow striations enable assessment of the model's ability to reconstruct small changes in surface topography.

Photos were taken using a dedicated mirrorless camera (Olympus OM-D E-M5 Mk. III with an M.Zuiko Digital ED 60 mm f/2.8 Macro lens providing a 16.5° horizontal, 120 mm full-frame equivalent field of view (Olympus Corporation 2019)) and a smartphone (Google Pixel 7 Pro using the inbuilt telephoto lens providing a 17.5° horizontal, 116.2 mm full-frame equivalent field of view (Google 2025)). On the dedicated camera, an aperture of f/4 — the sharpest aperture for this lens (DXOMARK 2012) — was selected. As this aperture produced a depth of field too narrow for the entire sample to be acceptably in focus, the images were focus-stacked from 20 individual exposures using Helicon Focus Pro (Gallo *et al.* 2014; HeliconSoft 2023) to ensure the entire sample was acceptably sharp. Shutter speed was varied to balance the exposure and is not expected to have had an influence on image quality due to the inanimate subjects and stationary cameras. A tripod and remote shutter release were used to minimise camera shake. Photographs were recorded in both JPEG and RAW (ORF) formats for comparison between the results of these formats. Most images were taken using the base native ISO of 200 (Olympus Corporation 2019; Claff 2025); however, to study the effect of ISO and digital noise on model quality, photographs of the marble sample were additionally taken at the maximum ISO of 25600, notably higher than typically recommended for photogrammetric surveys (Historic England 2017; O'Connor 2018; Howell *et al.* 2021). The "OpenCamera" app (Harman 2025) was used on the smartphone to enforce the use of the telephoto lens; however, this app did not allow the recording of RAW images or manual control of ISO and so these were not varied in this experiment. The smartphone camera has a fixed aperture, and the depth of field was sufficiently large (5 – 7 cm at 0.75 – 1 m focal distance) that focus stacking was not required for the entire sample to be acceptably sharp.

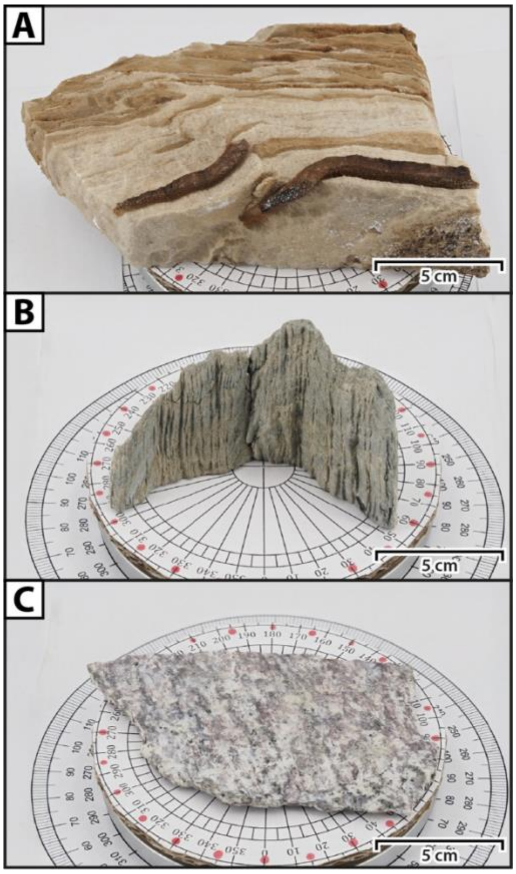

Figure 2: Rock samples photographed in this study. A) Marble with flanking folds. B) Folded schist. C) Granite fracture surface.

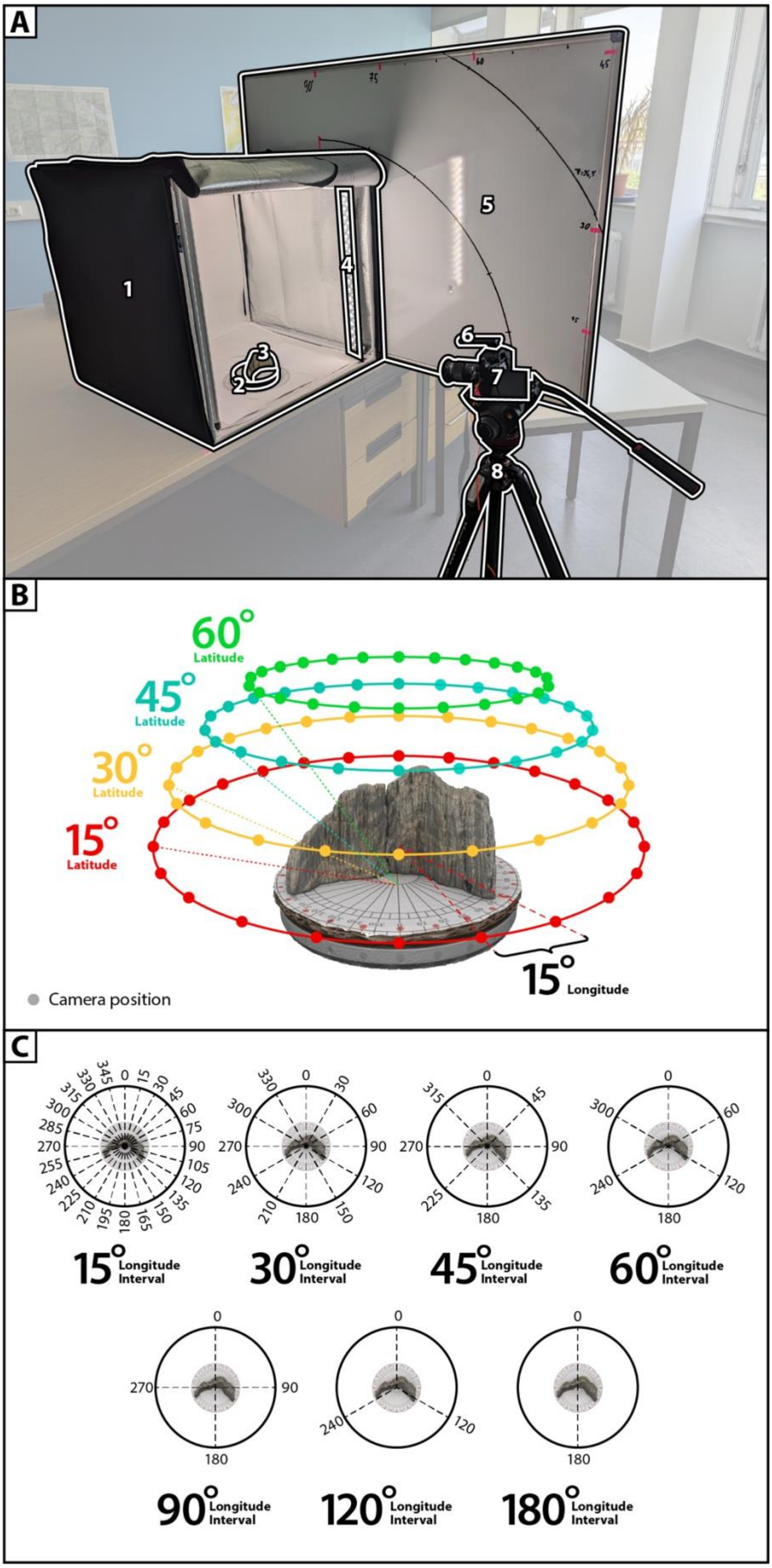
A
1
2
3
4
5
6
7
8
B
60° Latitude
45° Latitude
30° Latitude
15° Latitude
15° Longitude
Camera position
C
15° Longitude Interval
30° Longitude Interval
45° Longitude Interval
60° Longitude Interval
90° Longitude Interval
120° Longitude Interval
180° Longitude Interval

Figure 3: Image acquisition setup. A) Camera set-up showing the light-box (1), turntable (2), sample (3), one of the light sources (4), whiteboard indicating latitude angle (5), remote shutter release (6), camera and lens (7), tripod (8). B) Camera positions within each orbit showing the latitudes of each orbit. Photos were taken every 15° of longitude around each orbit. C) Camera positions used for each longitude interval. Sample size and working distances not to scale.

A light-box was used to ensure consistent lighting and a tripod and turntable were used to ensure a structured camera network (Fig. 3A). Working distances between 71 cm and 98 cm were selected such that the sample filled the image frame and were held constant for each sample and camera choice. The samples were rotated on the turntable in 15° increments through 360° to simulate an orbit with 24 camera positions. Four orbits were performed for every sample by varying the angle of pitch of the camera relative to the turntable stage while maintaining a constant working distance to the centre of the turntable. The camera network therefore forms a hemisphere around the centre of the stage as the turntable is rotated (Fig. 3B); in this study, we describe rotations of the turntable as "longitude" and the angle of pitch away from horizontal as "latitude". To assess different camera network configurations, the image dataset was subdivided into different combinations of latitude orbits (Fig. 3B); these were further subdivided into increments of different longitude angles between adjacent images (Fig. 3C). Eleven latitude combinations were tested: 1) [60°, 45°, 30°, 15°]; 2) [60°, 45°]; 3) [60°, 30°]; 4) [60°, 15°]; 5) [45°, 30°]; 6) [45°, 15°]; 7) [30°, 15°]; 8) 60°; 9) 45°; 10) 30°; 11) 15°. Additionally, for every latitude combination, seven sets of longitude intervals were considered: 1) 15° longitude intervals (24 photos per orbit); 2) 30° longitude intervals (12 photos per orbit); 3) 45° longitude intervals (8 photos per orbit); 4) 60° longitude intervals (6 photos per orbit); 5) 90° longitude intervals (4 photos per orbit); 6) 120° longitude intervals (3 photos per orbit); 7) 180° longitude intervals (2 photos per orbit). For each unique combination of camera position, ISO value, recording format, and camera, three near-identical images were taken in each setting to evaluate the consistency of results, resulting in a total of 3168 images (46,944 individual exposures before focus stacking). In total, 2541 models were included in this study.

Photogrammetric models were constructed using Agisoft Metashape Pro (version 2.0.4) (Agisoft 2023) on a computer with an AMD Ryzen 9 PRO 5945 CPU, an NVIDIA RTX 3080 GPU, and 64 GB of RAM. Marker points were manually selected on the photos to allow alignment of the models after model creation. "Alignment accuracy" was set to "high" to process the images without upscaling or downscaling and "exclude stationary tie points" was selected to avoid inclusion of parts of the scene not on the turntable. “Model quality” was set to “ultra high” to process the images at their original resolution and “face count” was set to “high” to ensure detail was not lost in decimation of the model (Agisoft 2025). “Interpolation” was disabled and “depth map filtering” was set to “mild”.

2.2. Evaluation of Photogrammetric Results

To quantify the relative influence of camera network design, ISO, image format, and camera choice on the quality of photogrammetric models, we systematically evaluated the results of image alignment, subjective model quality, and similarity to a reference model.

2.2.1. Image Alignment

Image alignment was evaluated by comparing the reconstructed placement of each camera against its known position. This comparison was achieved by measuring the mean inverse Euclidean distance between reconstructed camera placements and known camera positions (Eq. 1). To determine the known camera positions, we took all of the camera positions from the models derived from images taken at 60°, 45°, 30°, and 15° latitude and 15° intervals of longitude using ISO 200 — 6 models for the dedicated camera, 3 for the smartphone — and averaged the positions of each of the cameras. In the case where individual cameras were visibly misplaced in these models, the positions of these cameras were taken from another model where the positions were correctly reconstructed. Where a camera failed to be aligned by Metashape and would therefore not contribute to the model, it was assigned a distance value of infinity. The inverse of the distance was chosen in order to allow the calculation of an average distance metric in a dataset that contained infinities.

$$\mathrm{AID} = \frac{1}{N}\sum_{i=1}^{N}\frac{1}{\|\boldsymbol{k}_i - \boldsymbol{r}_i\|_2}$$

*Equation 1: Average inverse Euclidean distance (AID) between the known camera positions (**k**) and the reconstructed camera positions (**r**), both represented as 3D vectors. Where no corresponding reconstructed camera position exists, the Euclidean distance becomes infinity. N refers to the number of camera positions.*

2.2.2. Model Quality

Model quality was evaluated using a holistic subjective quality rating referred to here as the “model quality rating”. This is a number between 0 and 6, where 6 denotes a near-perfect model and 0 denotes failure to reconstruct any recognisable part of the sample. This rating was assigned by visual inspection of the models and comparison with the physical samples. Integer points were deducted from a perfect ranking due to the presence of the following five flaws (Fig. 4): A) smoothing or surface noise, either in the form of bumps or clusters of holes, B) more than approximately 20% of the model being missing, C) extraneous geometry, e.g., duplicate surfaces, D) stretched or sheared geometry, E) misaligned sections of the model. An additional point was deducted if any of the above flaws were so severe as to render the model unrecognisable as the sample or if a model failed to be built. This subjective assessment was conducted by one worker over a period of three weeks to ensure consistency.

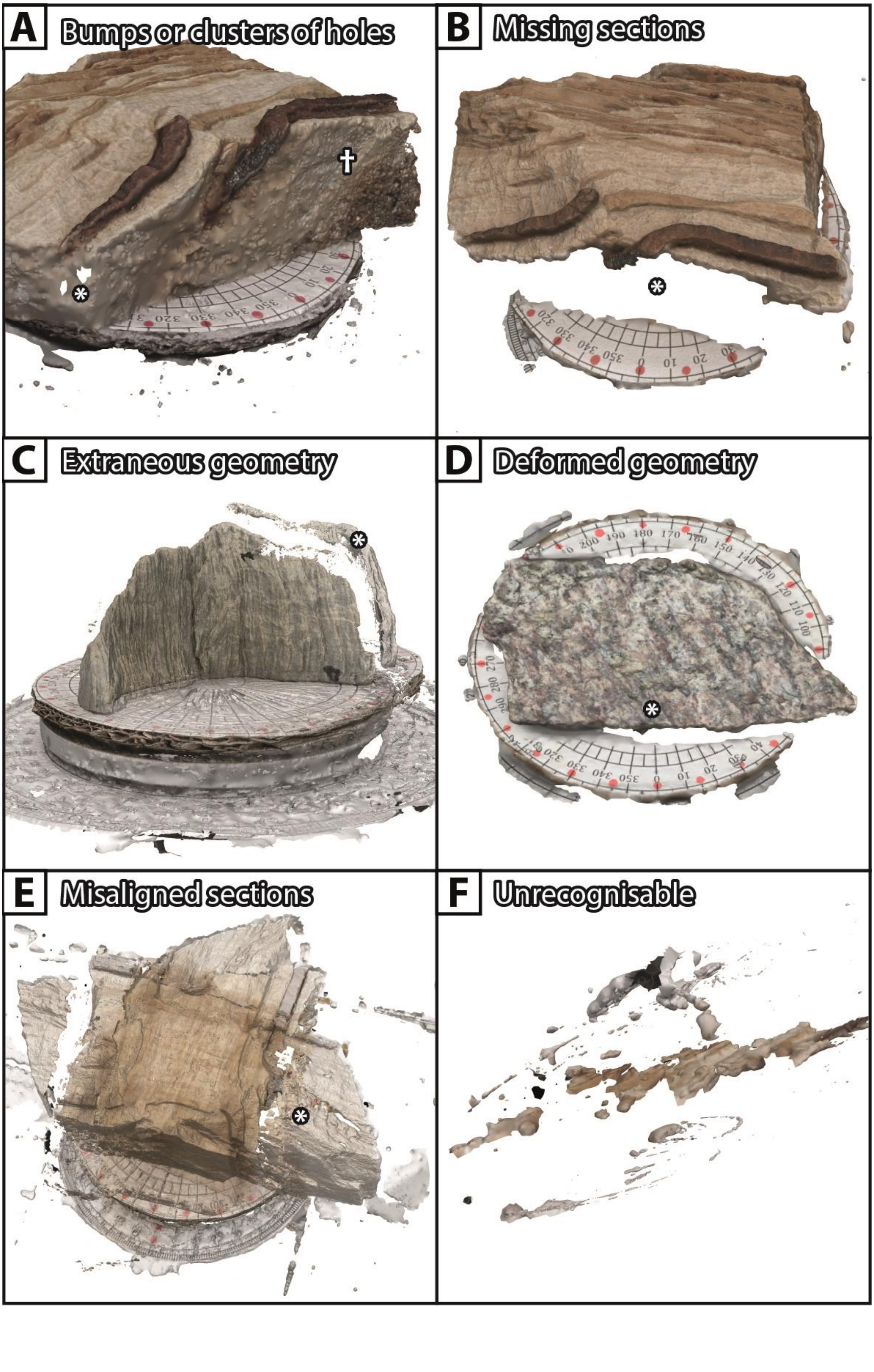
A
Bumps or clusters of holes
B
Missing sections
C
Extraneous geometry
D
Deformed geometry
E
Misaligned sections
F
Unrecognisable

Figure 4: Examples of models which clearly display the flaws that count against the model quality rating. A: Model exhibits small holes (*) and erroneous bumps (†) across the surface. This model received a quality rating of 4. B) Model missing an entire side of the sample (*). This model received a quality rating of 5. C) Model contains extraneous geometry (*). This model received a quality rating of 3. D) Model showing a deformed representation of the sample which is stretched along the horizontal axis (*). This model received a quality rating of 3. E) Model shows a duplicate section of the sample (*) rotated at ~90° to the rest of the sample. This model received a quality rating of 1. F) Model is entirely unrecognisable as the sample. This model received a quality rating of 0.

In addition to the model quality rating, the similarity of each model to a reference model was evaluated using the root mean squared error (RMSE) of cloud-to-mesh distances. To construct the reference model — similar to the known camera positions — we took all of the models derived from images taken at [60°, 45°, 30°, 15°] latitude and 15° intervals of longitude using ISO 200 — 6 models for the dedicated camera, 3 for the smartphone — and averaged the positions of each of their vertices. The cloud-to-mesh distance was computed by identifying the coordinates of corresponding points on both meshes by projecting rays along the vertex normals. We then calculated the root mean squared error (RMSE) between each compared model and the reference model for every point on the mesh.

3. Results

3.1. Camera Positions

The photogrammetric models constructed displayed a range of model qualities (Fig. 5). Comparison between models created using images from different positions shows that, for all samples, cameras (dedicated camera or smartphone) and camera settings (ISO and image format), shorter longitude intervals and higher latitude orbits result in both improved camera positioning (Fig. 6) and model quality (Fig. 7 and Fig. 8). Models derived from orbit combinations containing images taken at steep orbits (e.g., 60° latitude) generally outperform models derived from images taken at shallower latitude angles. Models derived from high latitude images display good reconstructions of the top surface while the sides of the samples and areas beneath overhangs are poorly reconstructed. Conversely, models derived from low latitude images show well-reconstructed sides and flaws are instead concentrated on the top surface of the sample (Fig. 5). At higher latitudes, fewer images and greater longitude intervals are sufficient to obtain good quality results (model quality rating greater than or equal to 5). Above 30° longitude intervals, models with a quality rating equal to or less than 1 are common. A deviation from this pattern is seen in the [60°, 45°] latitude and the [60°, 45°, 30°, 15°] latitude camera networks where longitude intervals of 90° or greater are more poorly reconstructed than in the [60°, 30°] latitude and the [60°, 15°] latitude camera networks. This effect is much less pronounced for the granite sample, which was flatter and for which the top of the sample was always clearly visible, even at 15° latitude. 15° longitude intervals produced reliably good camera positioning and good quality models for all combinations of orbit latitudes in all but a handful of cases (e.g., the marble sample at 15° latitude with JPEG images [Fig. 7]). For greater longitude intervals, reconstruction of the camera positions and model quality improve for combinations of orbits that include higher latitude orbits when compared with those containing only lower latitude orbits. Camera positioning and model quality also improve with an increased number of orbits which give sufficient coverage to enable good reconstructions from all angles. Model quality generally correlates with camera positioning as poorly aligned images preclude the creation of high-quality models; however, good camera positioning does not guarantee a high-quality model and in several instances poor quality models result despite well-positioned cameras (e.g., the schist sample at 60° latitude and 60° – 90° longitude intervals taken with the dedicated camera [Figs. 6 & 7]). Figures 7 and 8 show good agreement between the subjective model quality rating and the average inverse distance between each compared model and a reference model.

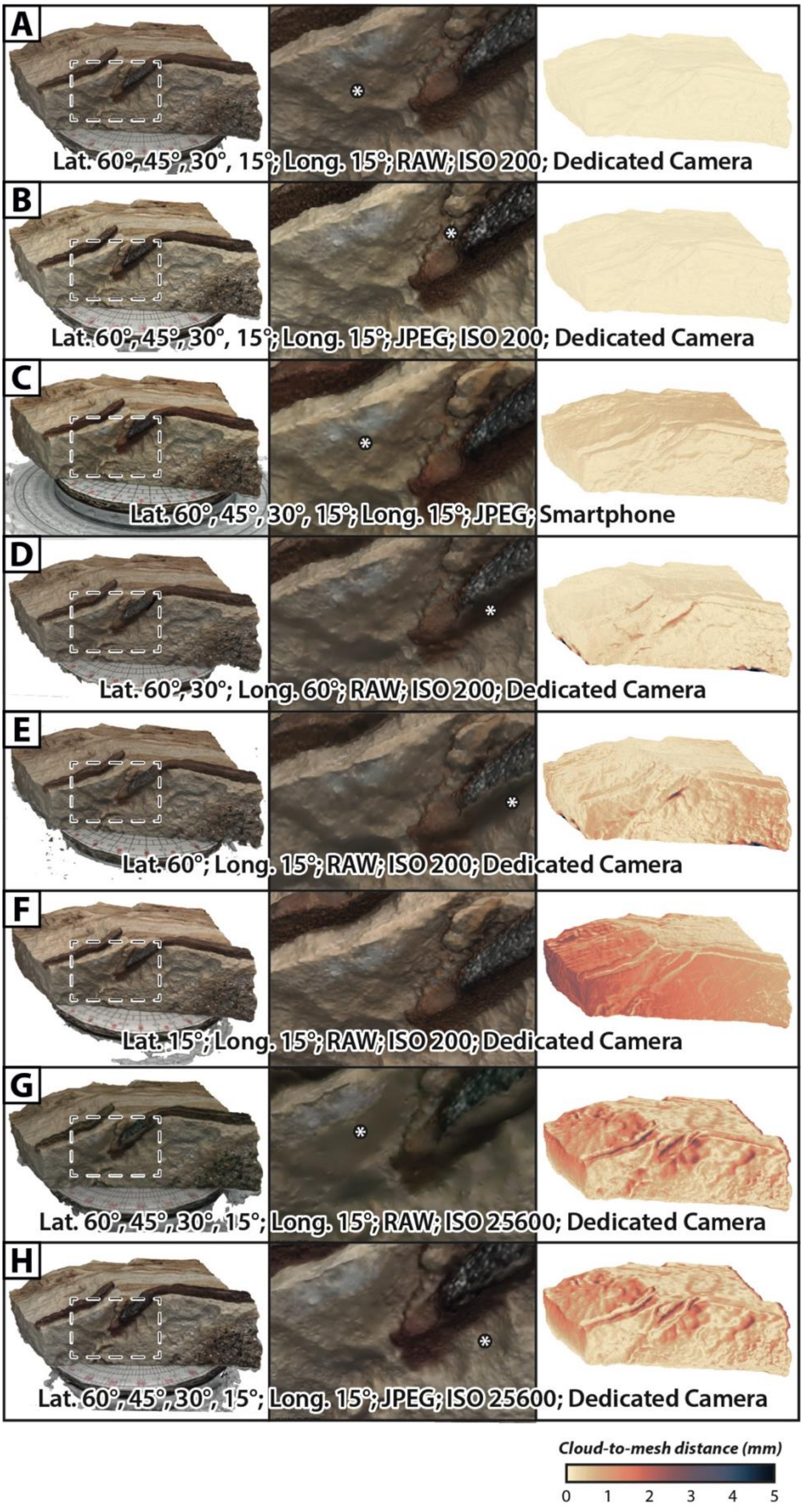
A
Lat. 60°, 45°, 30°, 15°; Long. 15°; RAW; ISO 200; Dedicated Camera
B
Lat. 60°, 45°, 30°, 15°; Long. 15°; JPEG; ISO 200; Dedicated Camera
C
Lat. 60°, 45°, 30°, 15°; Long. 15°; JPEG; Smartphone
D
Lat. 60°, 30°; Long. 60°; RAW; ISO 200; Dedicated Camera
E
Lat. 60°; Long. 15°; RAW; ISO 200; Dedicated Camera
F
Lat. 15°; Long. 15°; RAW; ISO 200; Dedicated Camera
G
Lat. 60°, 45°, 30°, 15°; Long. 15°; RAW; ISO 25600; Dedicated Camera
H
Lat. 60°, 45°, 30°, 15°; Long. 15°; JPEG; ISO 25600; Dedicated Camera
Cloud-to-mesh distance (mm)
0
1
2
3
4
5

Figure 5: Selected photogrammetric models demonstrating successful reconstructions. A) Model constructed from ISO 200 RAW images at [60°, 45°, 30°, 15°] latitude with 15° longitude intervals displaying one of the highest quality results achieved in this study (model quality rating = 6). Small details without much colour contrast are reconstructed but difficult to see (*). B) Model constructed from ISO 200 JPEG images at [60°, 45°, 30°, 15°] latitude with 15° longitude intervals displaying another of the highest quality results achieved in this study (model quality rating = 6) with improved definition of small details (*). C) Model constructed from smartphone images at [60°, 45°, 30°, 15°] latitude with 15° longitude intervals showing a high quality model with overall less definition (*) than the equivalent models from the dedicated camera (model quality rating = 6). D) Model constructed from ISO 200 RAW images at [60°, 30°] latitude with 60° longitude intervals showing good but not flawless results (model quality rating = 6). Some overhanging regions of the model show no detail (*). E) Model constructed from ISO 200 RAW images at 60° latitude, with 15° longitude intervals showing poor reconstruction of overhanging regions (*) (Model quality rating = 6). F) Model constructed from ISO 200 RAW images at 15° latitude, with 15° longitude intervals showing good surface reconstruction but an inaccurate overall geometry (model quality rating = 6). G) Model constructed from ISO 25600 RAW images at [60°, 45°, 30°, 15°] latitude with 15° longitude intervals displaying a complete but imperfect reconstruction (model quality rating = 4) with many regions across the whole model lacking detail (*). H) Model constructed from ISO 25600 JPEG images at [60°, 45°, 30°, 15°] latitude with 15° longitude intervals displaying a good but not flawless reconstruction (model quality rating = 5) with reduced detail (*) compared to the model derived from ISO 200 images.

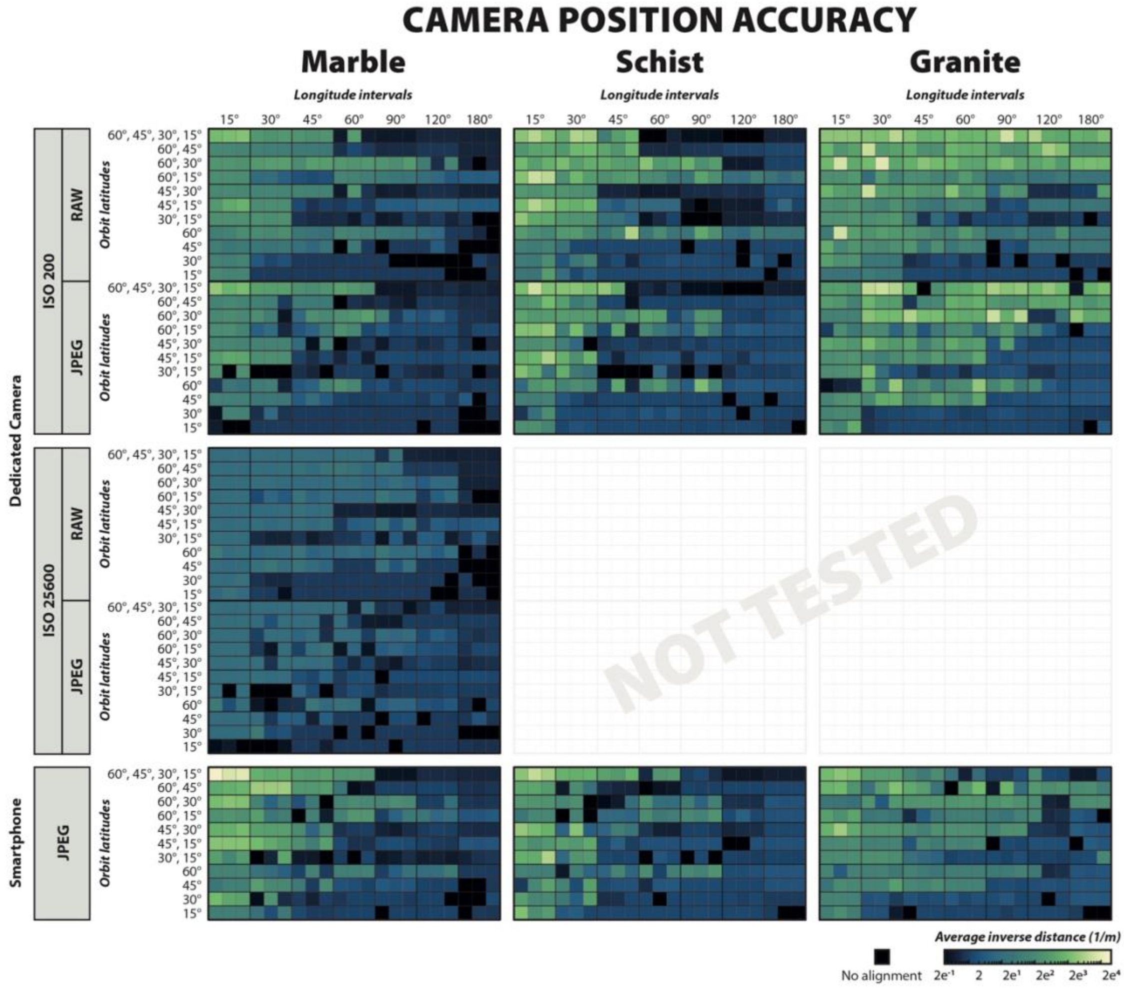

Figure 6: Average inverse distances between the known camera positions and the reconstructed camera positions for all models constructed (Eq. 1). Higher values correspond to smaller differences between the known and reconstructed camera positions and therefore better camera position estimates. Each coloured square represents one model and the colour of the square shows the average inverse distance for that model.

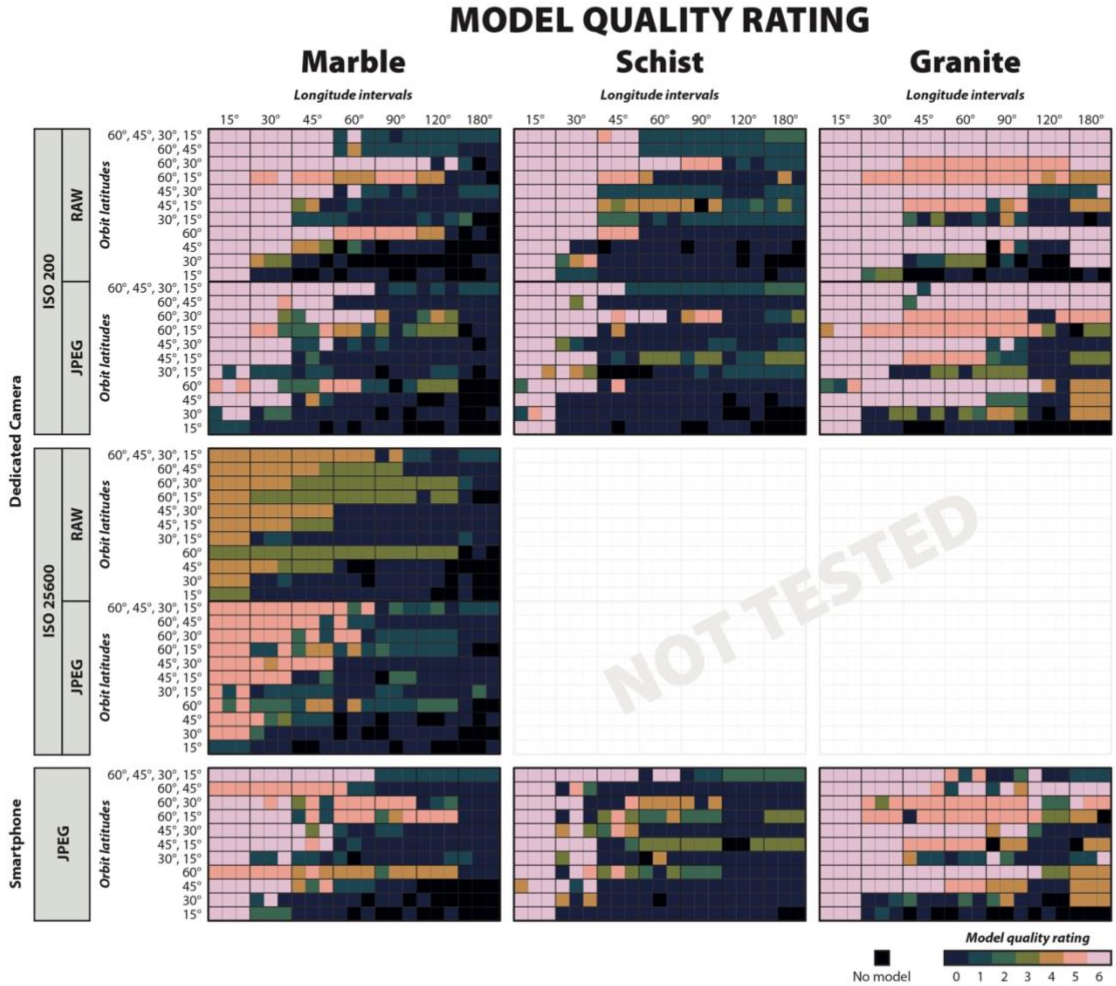

Figure 7: Model quality ratings for all models constructed. Each coloured square represents one model and the colour of the square shows the model quality rating for that model.

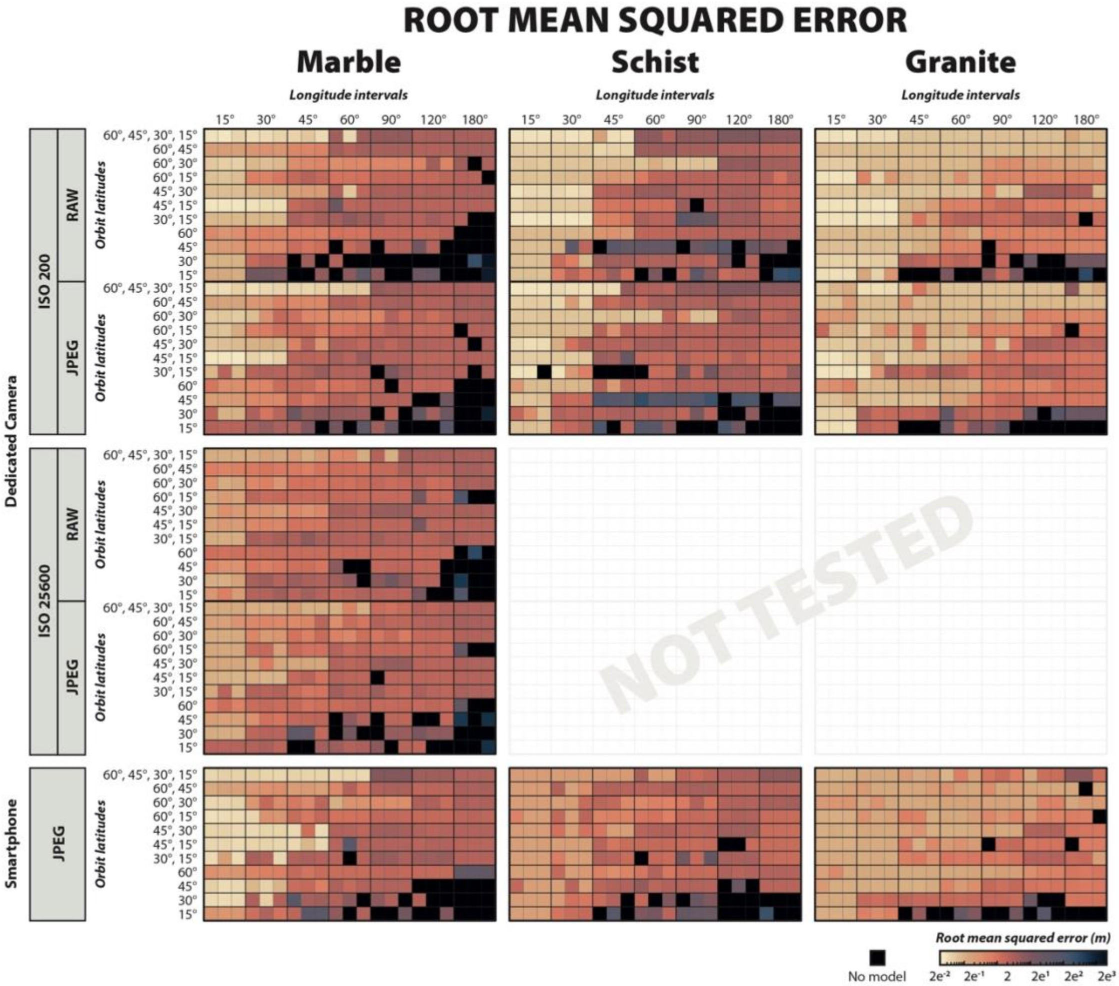

Figure 8: Root mean squared error between each model and the reference model for all models constructed. Each coloured square represents one model and the colour of the square shows the root mean squared error for that model.

3.2. Repeatability

As three models were created for each position and camera setting using near-identical images, this enabled us to investigate the repeatability of the photogrammetric process and the precision of its results. Multiple models produced from truly identical images were indistinguishable from one another. The near-identical images appear visually indistinguishable above the scale where individual pixels are visible and digital noise and compression artefacts can be seen. Despite this, both camera positioning and model quality results varied between models created from near-identical images. Figure 9 shows the standard deviation between the model quality ratings of models created from near-identical images. This shows that — in general — high latitudes and short longitude intervals produce the most consistently high-quality results; although models containing all orbits and the shortest longitude intervals do not necessarily display the most consistent results. Shallow latitude orbits and large longitude intervals produce consistently poor results. As such, intermediate longitude intervals and orbit latitudes produce the least consistent photogrammetric results. These results demonstrate that models created from JPEG images — especially those from the smartphone camera — had less repeatable results than those created from RAW images. The most consistent — but also poor-quality — results are derived from RAW images with high ISO that display the most digital noise of any images studied.

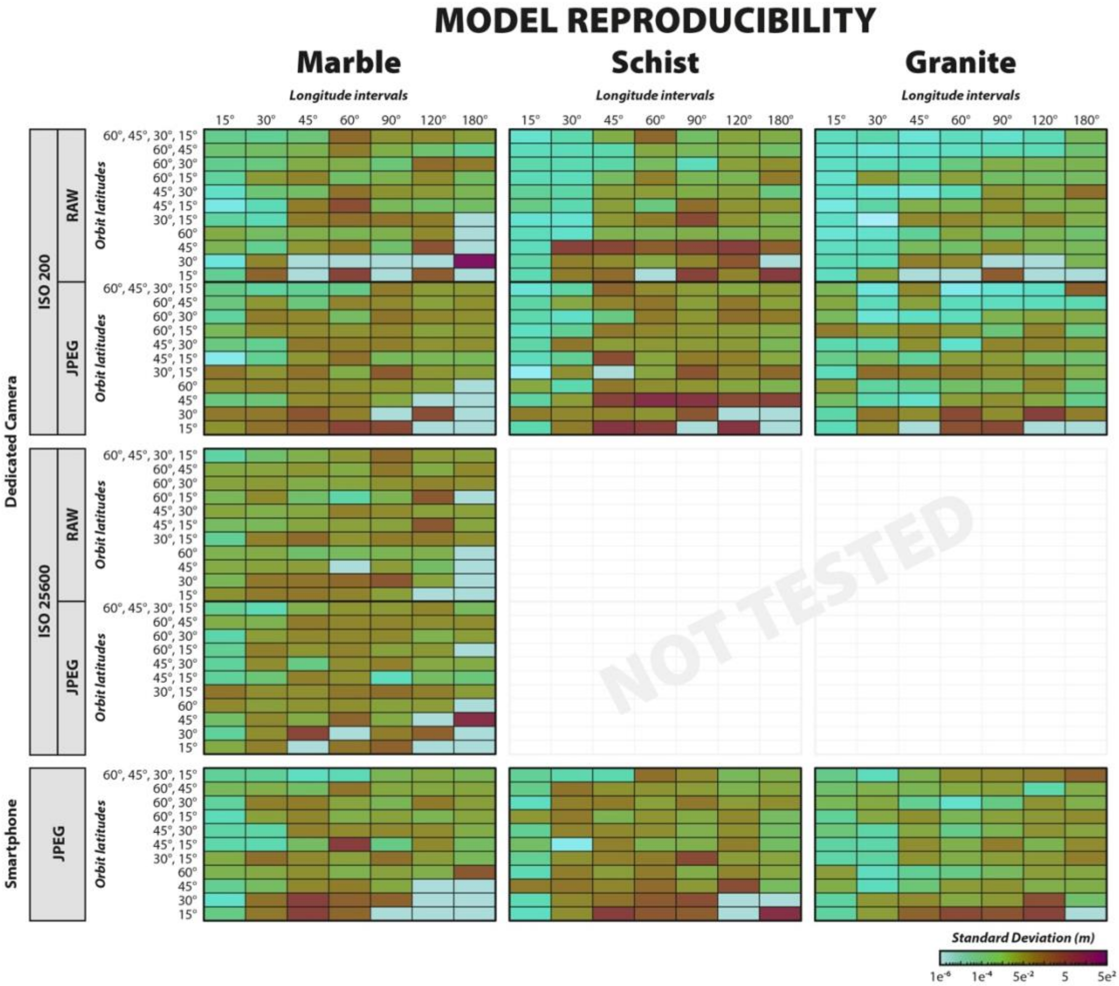

Figure 9: Standard deviations of root mean squared error for each position and camera setting. This shows a general pattern of more inconsistent results at greater longitude intervals and lower latitude orbits, whereas shorter longitude intervals and higher latitude orbits produce consistently good results (as seen in Figs. 7 and 8) and longer longitude intervals and lower latitude orbits produce consistently poor results.

3.3. ISO

These data show a clear influence of ISO — and of digital noise present in the high-ISO images — on photogrammetric model quality (Fig. 10) but a markedly smaller influence on the positioning of aligned cameras (Fig. 6). Models created from images taken at ISO 200 score — on average — 48% higher than models created from images taken at ISO 25600. No models derived from images taken at ISO 25600 scored the maximum model quality rating with models created from JPEG images scoring a maximum of 5/6 and models created from RAW images scoring a maximum of 4/6.

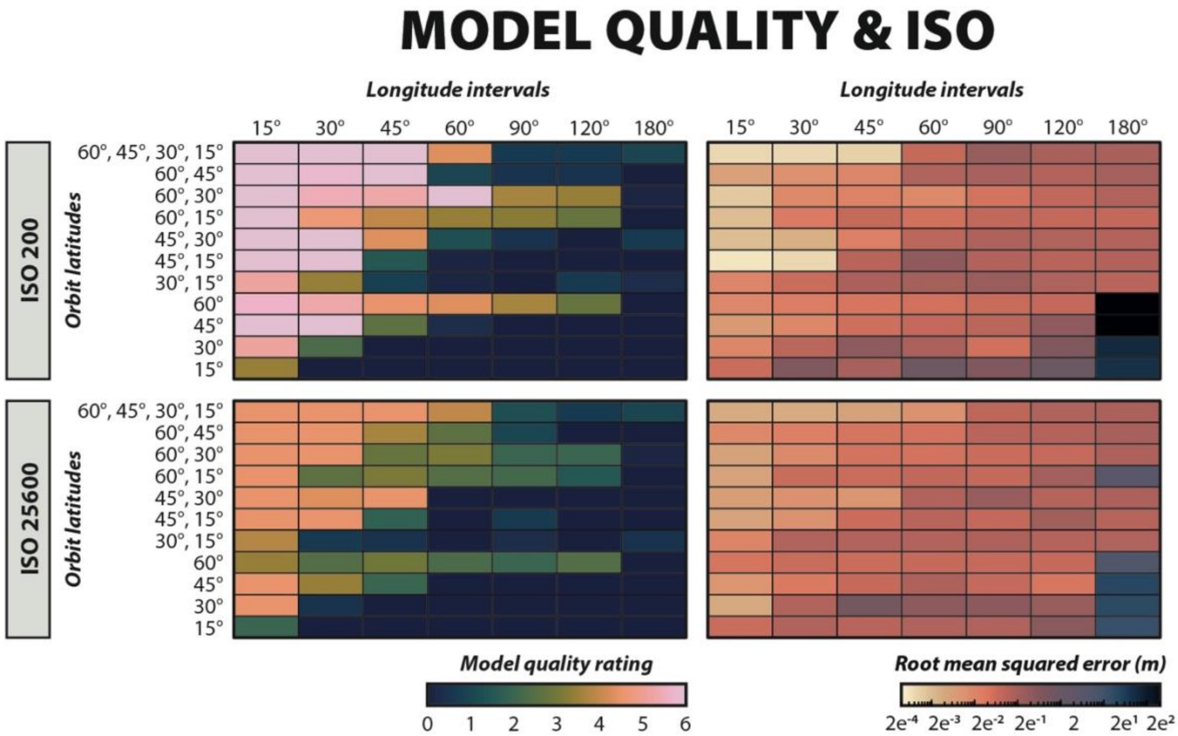

Figure. 10: Average model quality ratings and inverse distances for ISO 200 and ISO 25600 images. This shows data from the marble sample taken with the dedicated camera and averages together data from models derived from RAW and JPEG images. This demonstrates that images taken at low ISO produce notably higher quality models than images taken at high ISO.

3.4. Image Format

Models created from RAW images also outperform models created from JPEG images by 42% (Fig. 11). For models created from images taken at ISO 200, there was no difference in the maximum model quality rating between models created from RAW or JPEG images; however, RAW images produced more consistent results and the longitude interval after which model quality becomes poor (≤1) is greater for models created from RAW images than it is for models created from JPEG images. The photogrammetric process took — on average — 3 minutes and 5 seconds to process the JPEG images and 3 minutes and 51 seconds to process the RAW images.

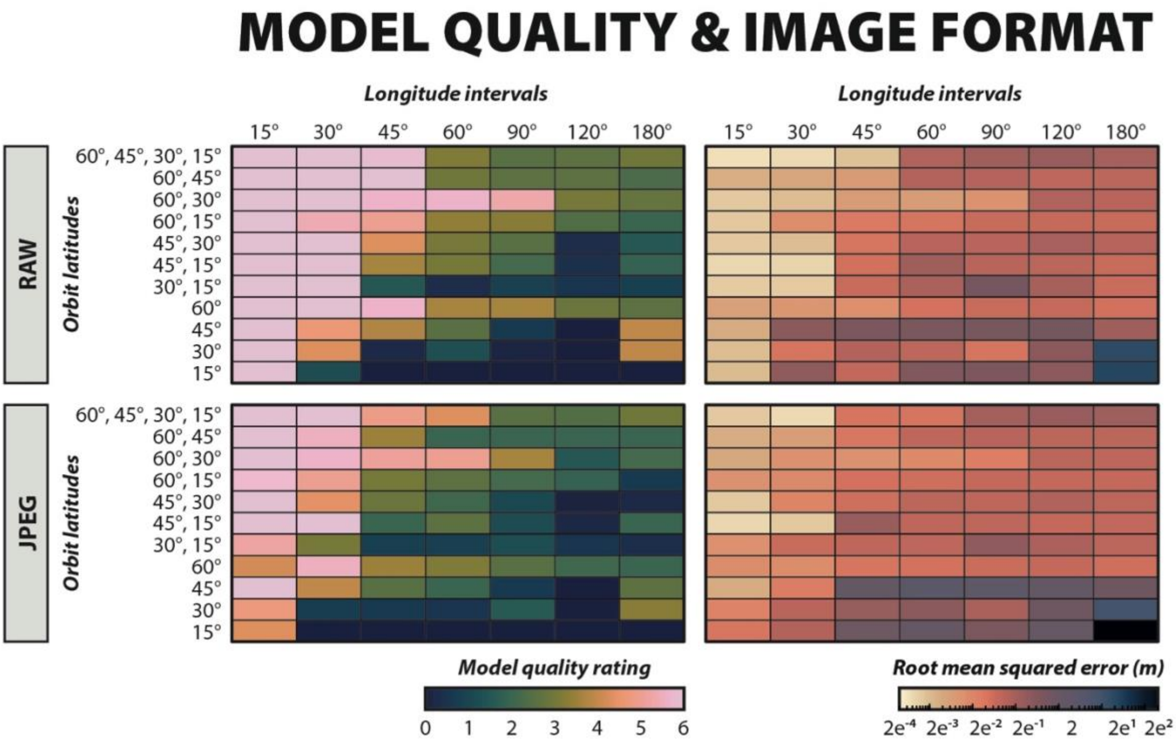

Figure 11: Average model quality ratings for RAW and JPEG images. This figure shows data for all samples taken on the dedicated camera at ISO 200 to ensure comparability. This demonstrates that models created from RAW images have an overall higher quality and that RAW images enable high-quality models to be produced from images taken at greater longitude intervals than JPEG images.

For models created from images taken at ISO 25600, despite RAW-derived models scoring a lower maximum model quality rating, all models outperformed equivalent JPEG-derived models at moderate – high longitude intervals. The longitude intervals after which model quality becomes poor (≤1) is similar between models derived from images taken at ISO 200 and ISO 25600.

3.5. Camera Choice

Models created from images taken with the smartphone performed similarly to those created from JPEG images taken with the dedicated camera. Specifically, models created from smartphone images outperform those created from JPEG images taken with the dedicated camera by only 9%, whereas RAW images from the dedicated camera outperformed JPEG images taken by the smartphone by 36% (Fig. 12). In fact, in various instances, models created from smartphone imagery outperform those created from dedicated camera imagery with the same camera network, although the consistency of these results is poorer.

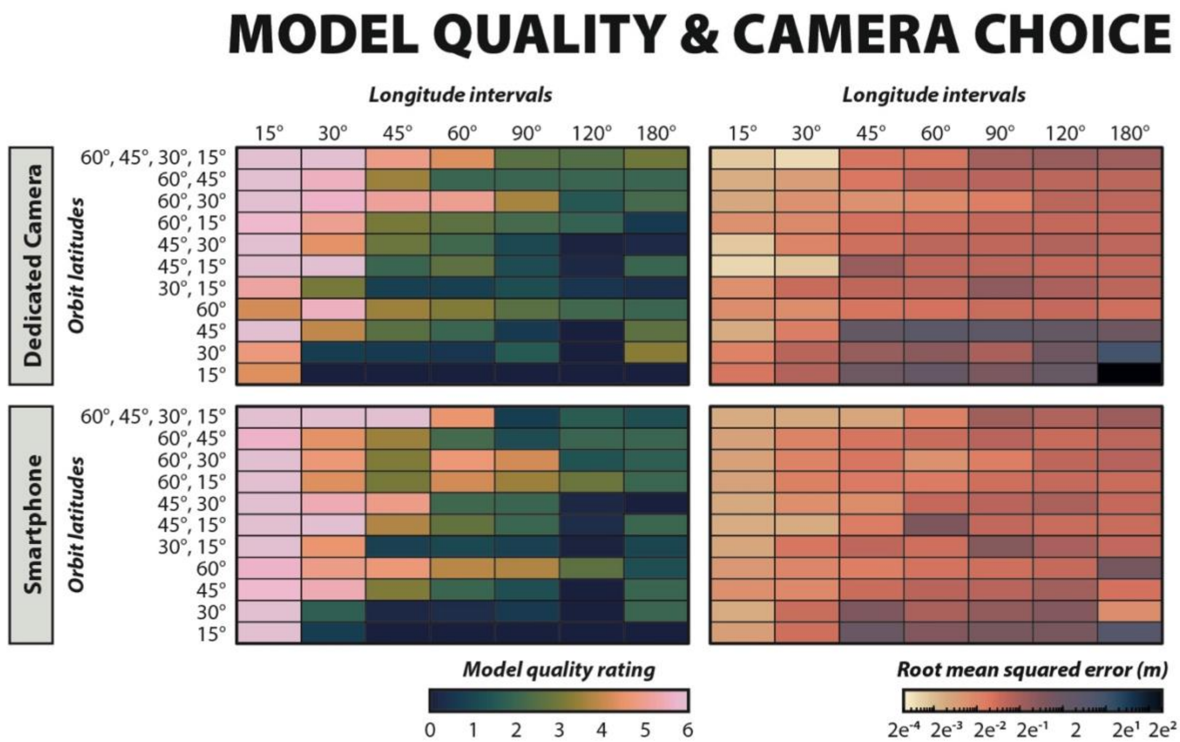

Figure 12: Average model quality ratings for images taken using the dedicated camera and the smartphone. This figure shows data for all samples and, for the dedicated camera, only includes images taken at ISO 200 to ensure comparability with the smartphone camera. This demonstrates that the average quality of models produced from smartphone imagery is similar to those produced from dedicated camera imagery.

4. Discussion

The observed pattern of model quality resulting from images taken at different latitude and longitude combinations and with different camera settings indicates the importance of considered photogrammetric survey design for the quality of resultant models. However, in order to discern practical guidance from these results, the underlying causes of sub-optimal model quality must be understood. In this discussion, we therefore examine the mechanisms behind how camera position, ISO, image format, and camera choice control the quality of resultant models and distil guidance for photogrammetric practitioners.

This study found no discernible influence of the sample's surface texture on photogrammetric results. All samples were opaque with an overall dull lustre and only a small proportion of vitreous (e.g., quartz) or pearly (e.g., mica) mineral grains. As such, the influence of other lustres or transparencies on photogrammetric model quality was not investigated by this study; however, techniques such as coating (Karami *et al.* 2022) or cross-polarised illumination (Bartoš *et al.* 2023; Clini *et al.* 2023) are well established means to overcome difficulties in reconstructing objects with these appearances. The results of this study are therefore most applicable to photogrammetry of rocks and stone — such as rock samples, fossils, outcrops, and worked articles of stone including buildings and statues — that typically exhibit irregular geometries, rough surfaces, and dull lustres without transparency.

4.1. Camera Position

The design of the camera network is demonstrated by this study to have the largest influence on photogrammetric model quality of any of the studied variables. Shorter longitude intervals — typically less than or equal to 30° — resulted in markedly higher quality models than those taken at greater longitude intervals. Image sets containing higher latitude orbits also resulted in improved model quality compared to those containing only shallow orbits. Additionally, models containing images taken at [60°, 45°, 30°, 15°] and the [60°, 45°] latitude combinations produced worse results at high longitude intervals than the models containing images taken at the [60°, 30°] latitude combination, despite the overall larger number of images in the first case.

The type and amount of distortion in 2D between the same point in two images depends on the difference in 3D real space between the directions of view of both camera positions. In our case, this means that the type and amount of distortion between adjacent image pairs depends on the difference in latitude and longitude. The lower the angle of latitude, the greater the angle between the rotational axis of the turntable and the optic axis of the camera.
A greater angle between these two axes results in a greater component of non-uniform scaling, skew, and perspective in the transformation between matched keypoints. This means that a rotation of a given longitude angle will introduce more non-rotational distortion at low latitudes

than at high latitudes (Fig. 13). Feature descriptors may be tolerant to some changes in shape between matched keypoints but such distortions do impact the similarity of these matches (Moreno-Noguer 2011). As such, keypoints in a matched image pair at a low latitude will look more different from each other than those in a similar image pair at a higher latitude, given the same longitude offset. While it is not publicly known which feature descriptor is used by Agisoft Metashape — and therefore which types of distortion it is invariant to — invariance to perspective distortions remains a challenge for feature descriptors (Moreno-Noguer 2011; Yu and Morel 2011; Li *et al.* 2017; Yu *et al.* 2018; Wang *et al.* 2025).

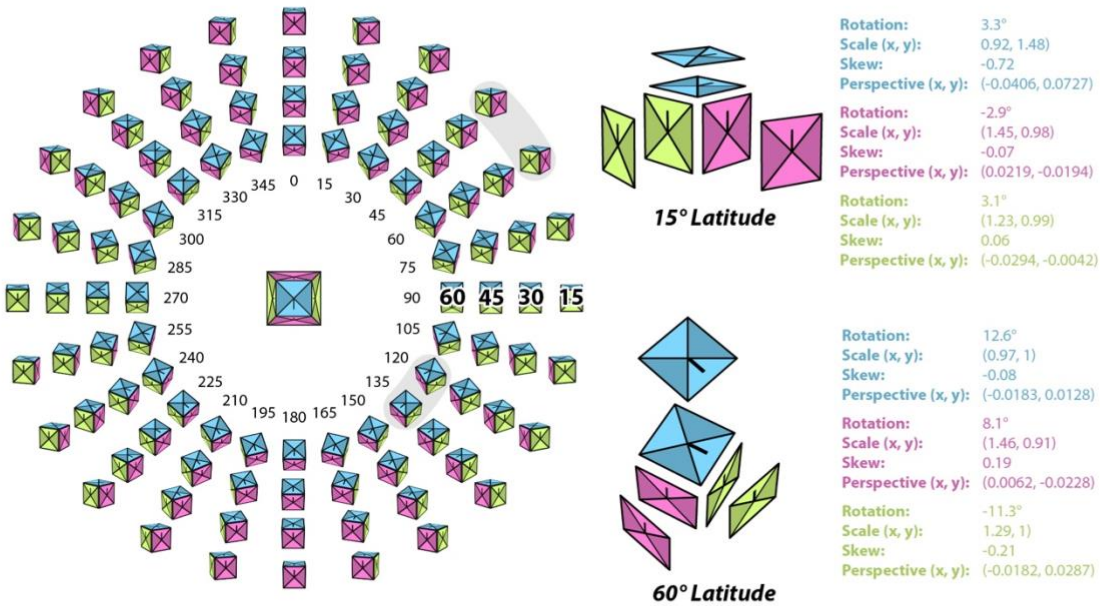

Figure 13: Demonstration of the perspective distortion seen between images at different camera positions illustrating the distortion that would affect all feature points on the sample. Each cube in the circle shows what the cube in the centre (shown in reverse perspective) would look like as seen from a camera at its position in the circle. The radial axis shows the latitude while the circumferential axis shows the longitude. Note that the top surface (blue) is visible throughout the entire orbit while each side (pink and green) is only visible for half the orbit. The top surface mostly undergoes rotation with only minor non-affine perspective distortion at 60° latitude, while at 15° latitude perspective distortion is dominant. The sides undergo strongly non-affine perspective distortion at all latitude angles.

To demonstrate this phenomenon, we developed an image matching and keypoint evaluation script using OpenCV (Culjak *et al.* 2012), Open3D (Zhou *et al.* 2018), and TriMesh (Dawson-Haggerty 2023) to interrogate the processes involved in matching features between images (Fig.

14). We used OpenCV for this task as Metashape does not allow full access to the attributes of matched points. We performed this analysis on one set of imagery: the marble sample photographed with the dedicated camera at ISO 200, RAW, and we used only one of the three near-identical sets of imagery. This script takes as input manually masked images to ensure that detected keypoints are on the object. Following this, SIFT keypoints are detected and matched pairwise between images. The Euclidean distance between the SIFT feature descriptor for each point — represented as a high-dimensional vector — and its matching point demonstrates the difference in the appearance between the same matched features in both images. The difference between each feature point and its best and second-best match are noted and, where the ratio between the best match and the second-best match is below 0.8, these points are considered too ambiguous and are therefore discarded (Lowe 2004). In order to evaluate whether matches are true or false positives, the position of each matched feature point was projected from known camera positions onto a pre-existing photogrammetric model of the object (Fig. 14A). We then compared the coordinates of these projected points and considered only points within 1 mm (0.5% of the length of the object) to be true positive matches. False positive matches were flagged as such and remained in the dataset for demonstration purposes, as can be seen marked in red in Fig. 14B.

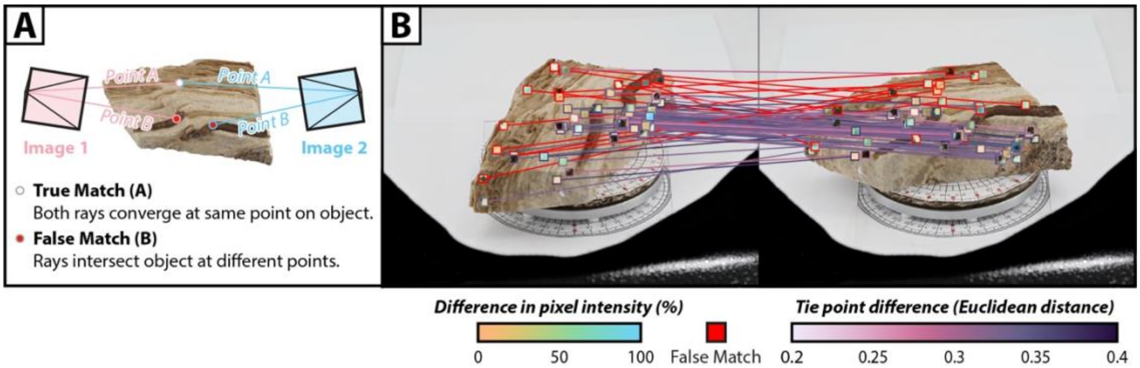

Figure 14: Analysis of the similarity and validity of matched feature points. A) Methodology for determining whether a match is a true or false positive using raycasting from the camera positions to a pre-existing model. B) Image pair showing difference (Euclidean distance between SIFT vectors) of matched keypoints. Each matched keypoint is shown as a tile representing the patch recognised by the SIFT feature descriptor with a coloured border and tie-line showing the difference between these matched points. Each tile shows a false-colour enlargement of the patch with oranges indicating similar greyscale intensity values between matched patches and blues indicating different intensity values. Red borders and tie-lines

indicate matches recognised as false positives. For demonstration purposes, only the top 100 matched points are shown.

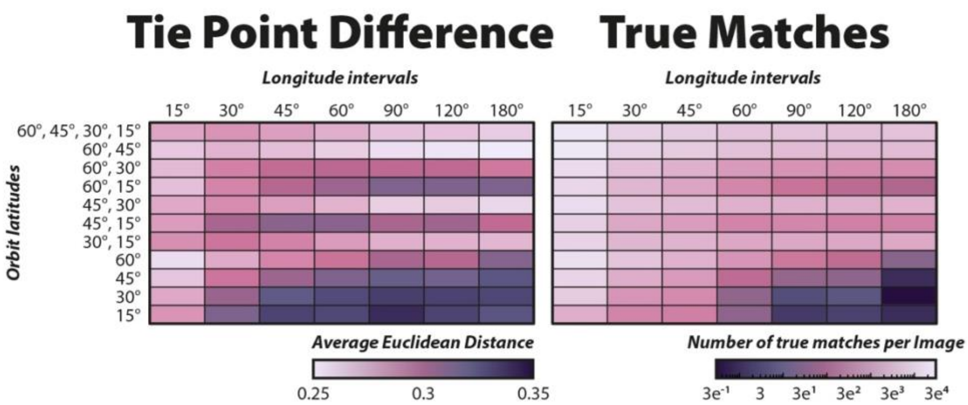

Figure 15: A) Average Euclidean distance between matched keypoints, and B) average number of true matches per image.

This analysis shows that the pattern of the average Euclidean distance between matched keypoints and the average number of true matches per image both reproduce the pattern of improved results with shorter longitude intervals and higher latitude orbits observed in the model quality analysis (Fig. 15). Matched keypoints in higher latitude orbits show a smaller Euclidean distance than matched keypoints in lower latitude orbits, thereby decreasing the risk of incorrect matching (Lowe 2004). For combinations of orbits, those containing higher latitude orbits similarly show smaller Euclidean distances and more true matches than combinations consisting of lower latitude orbits.

However, this analysis does not reproduce the observed poor results for the [60°, 45°] latitude combination and the [60°, 45°, 30°, 15°] latitude combination for longitude intervals of 90° or greater. This analysis also does not consider which images are matched together and the strength of those matches which together define the *connectedness* of the camera network. To address this, we constructed network graphs for all of the camera networks showing the number of true matches for each image pair (Fig. 16)(Cui *et al.* 2021; Xiao *et al.* 2021). To simulate the filtering process to determine which images are considered “aligned” by Metashape, we removed all image pairs where the number of true matches was less than 10% of the maximum number of true matches for any image pair in the network. This had the effect — as also seen in Metashape — where images that are considered aligned in some camera networks may not be considered aligned in others; namely that images with a moderate number of true matches may be considered aligned when the camera network consists only of images with similar numbers of true matches but, if the camera network contains an image pair with considerably more true matches, the images with only moderate numbers of true matches will not be considered aligned. This can be seen in Figure 16 where, at high longitude intervals, images in networks containing multiple orbits are aligned between orbits but not along orbits, whereas these same images are aligned in networks containing only one orbit. As such, the entire camera network is better reconstructed when images are taken at regularly spaced intervals and the inclusion of images that contain an anomalously high number of correctly matched keypoints can break the connections between otherwise aligned images.

Figure 16 also shows the stronger connections between images taken at higher latitudes as low latitude orbits often do not display a wholly connected camera network and instead display a camera network broken into multiple components. Any more than one component in the camera network denotes a significant failure of the camera alignment process. In contrast, high latitude orbits maintain their connectedness even at greater longitude intervals and, at moderate longitude intervals that lack the very high number of true matched points between images at 15° and 30° longitude intervals, images on opposite sides of the camera network may be connected.

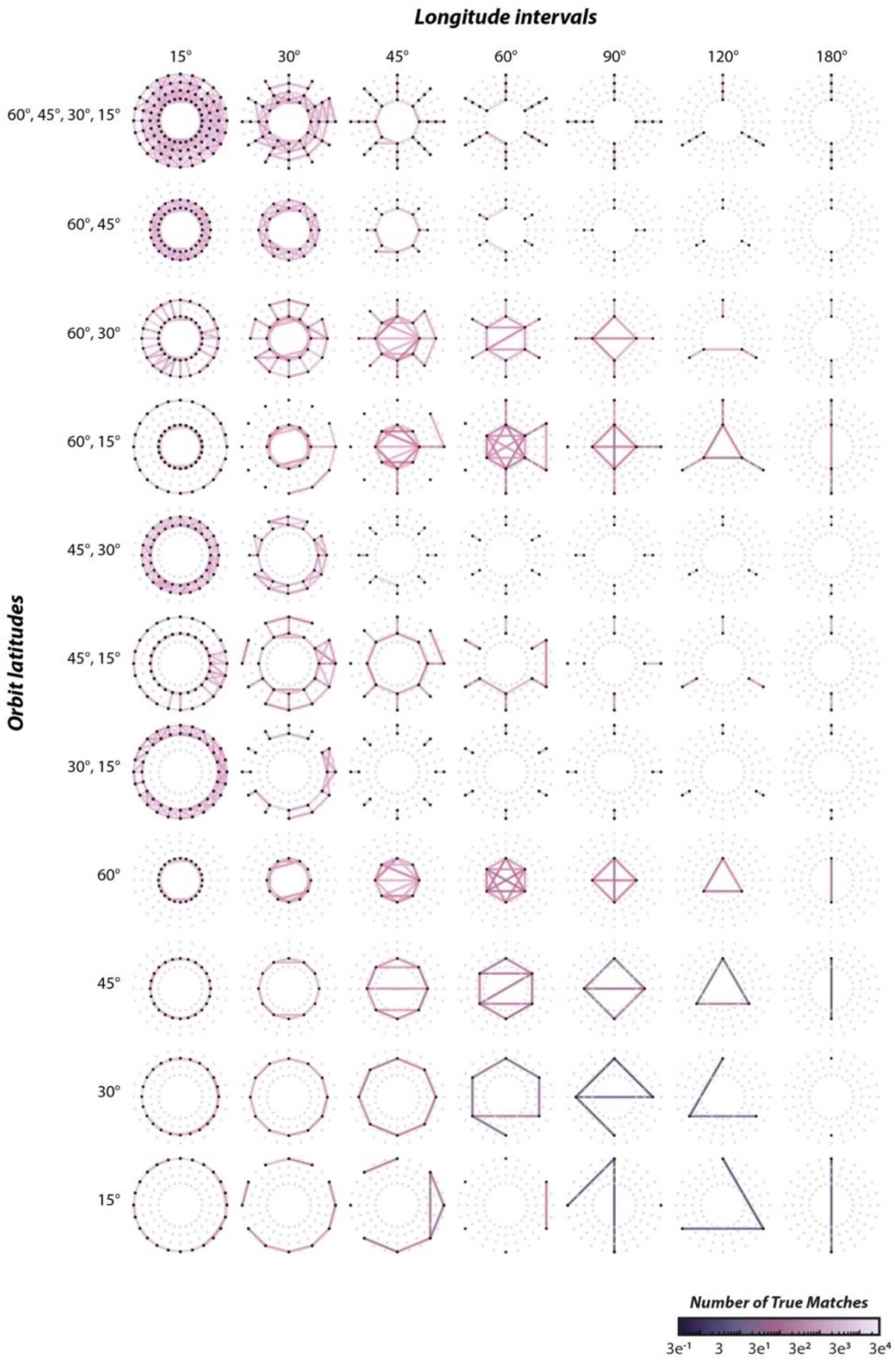

Figure 16: Network graphs showing matched image pairs (coloured lines) between different camera positions in each of the camera network configurations.

A disconnected camera network — i.e. one where a significant proportion of the images fail to be correctly aligned with the rest of the model and where unaligned portions consist of images that are related to each other in space — would prevent the information contained in those images from forming part of the model; detrimentally impacting the quality of the resulting model. We assessed the influence of these disconnected camera networks by calculating the average number of true matches per component in the camera network, with a component defined as a group of matched images with an unbroken path between the component members as shown in Figure 16. To ensure the camera network is appropriately penalised for being disconnected, we cubed the number of components. Figure 17 shows the pattern of true matches per component cubed; this pattern mirrors the pattern of camera positioning (Fig. 6) and model quality (Figs. 7 and 8). This shows both that camera networks consisting of higher latitude orbits contain more true matches per component than camera networks consisting of low latitude orbits — as was shown in Fig. 15B — and also that the [60°, 45°, 30°, 15°] latitude and [60°, 45°] latitude networks contain fewer true matches per component at high longitude intervals than the [60°, 30°] latitude networks as a consequence of the camera network being more disconnected. Additionally, this analysis shows that, at [60°, 45°, 30°, 15°] latitude and [60°, 45°] latitude, the number of true matches per component is higher at 180° longitude intervals than it is at 120° longitude intervals, which also matches the observations of model quality in these positions (Figs. 7 and 8).

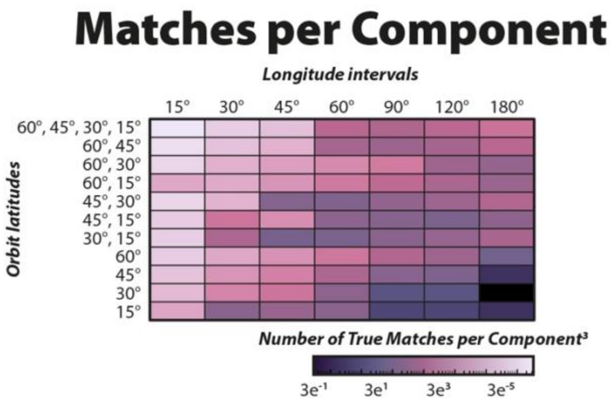

Figure 17: Average number of true matches between image pairs for each configuration of camera positions divided by the cube of the number of components. This shows a similar overall pattern as the camera position rating (Fig. 6) and subjective model quality rating (Fig. 7).

This analysis demonstrates the influence of 2D distortions — such as anisotropic scaling, skew, and perspective — on the success of feature matching and subsequent photogrammetric reconstructions. While feature descriptors such as SIFT can account for some distortion by virtue of their tolerances for differences between matched keypoints (Moreno-Noguer 2011), the large changes in perspective that result from high longitude intervals at low latitudes exceed the capabilities of feature descriptors to make correct associations between matched points. Additionally, our analysis of the influence of the connectedness of camera networks on photogrammetric results and how the presence of anomalously well-matched images can cause otherwise correctly matched images to fail to align demonstrates the importance of evenly spaced positions within camera networks.

As such, practitioners should avoid camera placements that include large changes in obliquity to an imaged surface without sufficient intermediate steps and should ensure that the spacing between camera positions is approximately even. For photogrammetric surveys using a turntable or where the camera network otherwise orbits an object of interest, practitioners should select short longitude intervals. A single high-latitude orbit is generally sufficient to reconstruct an object without overhanging regions or where the top surface is of primary importance; however, for objects with more complex geometries including overhanging regions, multiple orbits should be performed at sufficient latitudes to image all parts of the object. Where multiple orbits are used, the interval between camera positions in the latitude and longitude direction should be balanced so as to create an evenly distributed camera network.

The findings of this survey may also be applied to photogrammetric surveys which do not orbit an object of interest, such as for digital outcrop models. In these cases, the axis of rotation from one camera position to another will vary for each image; however, the same principle of minimising the perspective distortion between images can be applied. Surfaces should be imaged from camera positions where the optic axis of the camera is at a high angle to the surface. Where camera positions with the optic axis at a low angle to the surface are used — such as to ensure coverage of overhanging regions — sufficient intermediate steps between the high angle images and the low angle images should be taken.

4.2. ISO

The poor model quality resulting from the use of high-ISO images demonstrates the deleterious impact of digital noise on photogrammetric model quality. This result is in agreement with previous research (e.g., O'Connor 2018; Roncella *et al*. 2021) on the influence of digital noise on photogrammetric results. In uncontrolled lighting conditions, which are typical of geological photogrammetric surveys, ISO choice is typically a compromise with aperture and shutter speed to correctly expose the image, with large apertures risking parts of the scene being out of focus and slow shutter speeds risking motion blur, both of which are also well known to be detrimental to photogrammetric model quality (Sieberth *et al.* 2014a, b, 2015; Pan 2019; Sieberth 2020). This compromise may be made by the practitioner or may be managed by the automatic exposure controls, with many smartphone cameras not providing an alternative to automatic exposure.

The high-ISO JPEG images produced higher quality models than the high-ISO RAW images. This wasg due to in-camera noise-reduction post-processing which was applied to the JPEG images but which inherently cannot be applied to the RAW images (Fig. 18). This noise reduction was effective at partially mitigating the impact of high ISOs on photogrammetric model quality. The practitioner is therefore advised to select the lowest possible ISO value which balances the exposure without introducing out-of-focus or motion blur and to use noise reduction if necessary to improve image quality before the images are used in the photogrammetric process.

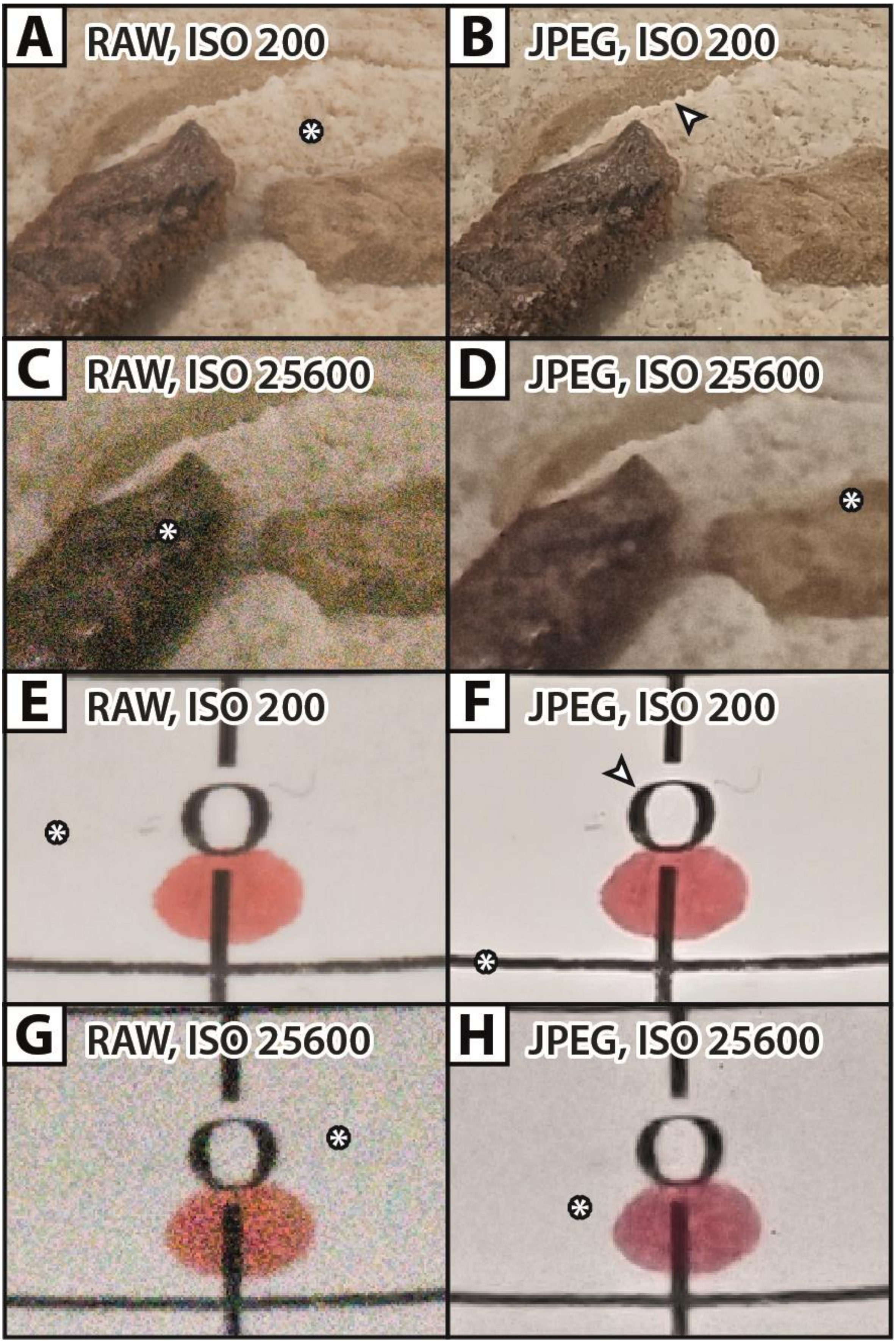

A
RAW, ISO 200
B
JPEG, ISO 200
C
RAW, ISO 25600
D
JPEG, ISO 25600
E
RAW, ISO 200
F
JPEG, ISO 200
G
RAW, ISO 25600
H
JPEG, ISO 25600

Figure 18: Digital noise and artefacts present in input images from the dedicated camera. A) Marble sample taken at ISO 200 RAW showing a low degree of digital noise and no artefacts from sharpening but lower contrast and clarity of features (*). B) Marble sample taken at ISO 200 JPEG showing light and dark fringing artefacts from sharpening (arrow) and small high contrast features are visible. C) Marble sample taken at ISO 25600 RAW showing a high degree of colour noise (*). D) Marble sample taken at ISO 25600 JPEG showing less digital noise than C but markedly reduced clarity (*). E) Turntable stage taken at ISO 200 RAW showing visible paper texture not present in other images (*). F) Turntable stage taken at ISO 200 JPEG showing light and dark fringing artefacts from sharpening (arrow) and paper texture in the white regions and the printed lines are replaced by solid colour blocks. G) Turntable stage taken at ISO 25600 RAW showing a high degree of colour and luminance noise (*). H) Turntable stage taken at ISO 25600 JPEG showing luminance noise visible in plain regions (*).

4.3. Image Format

This study also demonstrates that the use of RAW images as inputs into the photogrammetric process improves model quality over the use of JPEG images, while also improving the reliability of photogrammetric results. RAW images provide both increased bit-depth and a lack of post-processing (e.g. compression and sharpening) artefacts when compared with JPEG images. As shown in Fig. 18 and Fig. 19, sharpening artefacts as well as smoothing of low contrast areas obscure details that may be used as keypoints. However, at high ISOs, the high degree of digital noise in the RAW images also obscures features that are visible in the JPEG images which underwent noise reduction. However, processing RAW imagery took, on average, 41% longer than processing JPEG imagery.

When ISO is low and images are free from digital noise, practitioners may opt to use RAW images to improve photogrammetric results at the cost of increased processing time. However, in the case of noisy images such as those resulting from the use of a high ISO, noise reduction is shown to improve photogrammetric results and therefore JPEG images, which can preserve noise reduction results, are preferred over RAW images.

Figure 19: Contrast-enhanced images of the same exposure, saved as A) RAW and B) JPEG using on-camera processing. Note that mineral cleavage (arrow) is discernible in the feldspar crystal in the RAW image but is entirely obscured in the JPEG image where this crystal is rendered as a smooth surface. Note also that the contrast of edges is strongly enhanced in the JPEG image due to sharpening (*).

4.4. Camera Choice

In this study, the use of a dedicated camera provided a negligible improvement to the visual quality of photogrammetric results compared to the smartphone camera (Fig. 12). The 20-megapixel Micro-Four-Thirds sensor on the dedicated camera represents the low end of cameras with interchangeable lenses available at the time of this study. In contrast, the 48-megapixel quad-Bayer 1/2.55" sensor of the smartphone camera represents the mid-to-high end of smartphone cameras available at the time of this study. Figure 20 demonstrates the similarity in perceivable resolution between the two cameras. Printed lines in in-focus regions of the images show similar widths and acutances between both camera systems, with high-contrast lines appearing only slightly broader and the gradient of edges being only slightly less steep. The pattern of the JPEG images from the dedicated camera — while the same width as that from the RAW images when only considering pixels darker than the baseline — shows an overall deviation from the luminosity of the paper of similar width to that from the smartphone camera. The similarity in the quality of the images from these two cameras is likely responsible for the similarity in the precision of the camera positioning and the quality of the models between the products of these two camera systems.

A greater contrast between the capabilities of the two camera systems — such as the use of a dedicated camera with a larger and higher resolution sensor — may have yielded a greater difference between the results from these cameras. However, both smartphone cameras and dedicated cameras with Micro-Four-Thirds and APS-C-sized sensors are popular choices for geological fieldwork (Tavani *et al.* 2022), as smaller sensors usually result in a lighter camera body and lens and offer better stabilisation. Similarly, common consumer drones also have sensors comparable to both the smartphone and dedicated camera sensors used in this study (Olympus Corporation 2019; DJI 2021; Google 2025). As such, practitioners choosing to use smartphones or drones with small sensors are similarly capable of producing high-quality photogrammetric models as those choosing to use dedicated consumer cameras, assuming other parameters are equal.

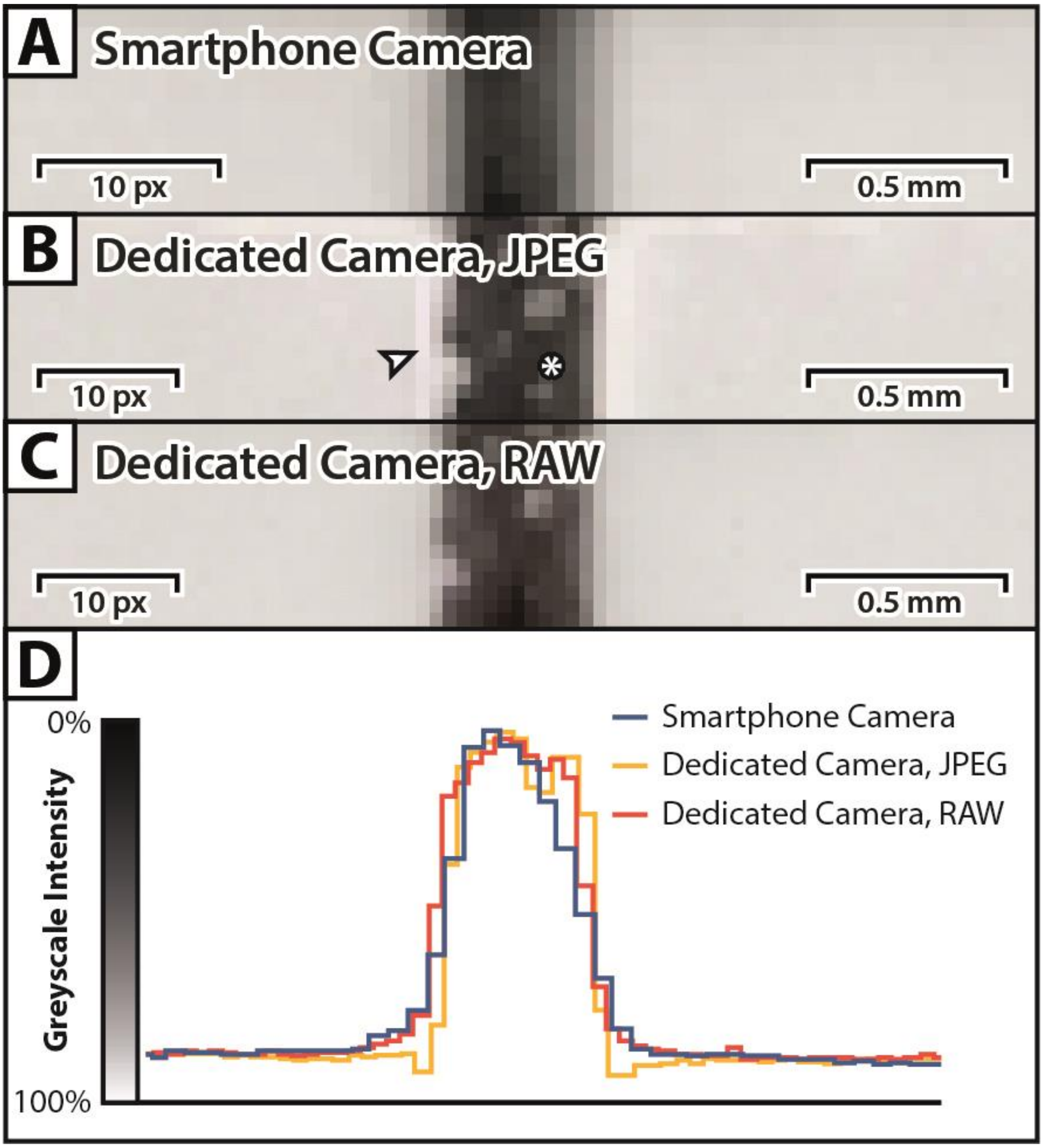

Figure 20: Comparison between the acutance of a printed line on the turntable stage in images from the smartphone camera and the dedicated camera. A) Image from the smartphone camera. Note the lack of texture in the printed line or the paper (*). B) JPEG image from the dedicated camera. Note the accentuation of small differences in luminosity (*) and the light-coloured fringing around high-contrast edges (arrow) as a result of sharpening. C) RAW image from the dedicated camera. Note the lack of sharpening artefacts and the subtle texture within the printed line and paper. D) Graph of the luminosity of each pixel across the profiles shown above with the exposure and contrast normalised. Note that the JPEG image from the dedicated camera shows the light-coloured fringing and accentuation of details from sharpening as seen in B.

4.5. Reproducibility

Despite the use of near-identical images, photogrammetric results between the three repetitions of each model are not consistent. The differences between these near-identical images are visually imperceptible; however, the patterns of digital noise and artefacts (e.g., from demosaicing, compression, and focus stacking) are different in every image and are at the scale of the feature descriptors used in image matching (Lowe 2004; Rublee *et al.* 2011). Features that may be uniquely distinctive in one image may not be in a near-identical image. This results in uncertainty of the quality of the photogrammetric model resulting from a given image set.

To investigate the differences between the photogrammetric results of near-identical images, we exported from Metashape the 2D coordinates of every matched point in every image pair and overlaid the points found in each image (Fig. 21). This demonstrates that, while some of the same points are matched between near-identical images, many matched points are only found in one of the images. The number of points found also differs between near-identical images. As shown in Figure 21, image pairs at a longer longitude interval contain significantly fewer matched points than those at a shorter longitude interval and contain proportionally fewer points in common between image sets. Therefore, image pairs containing fewer matched points displayed fewer overlapping points. Additionally, as images are added sequentially to the photogrammetric reconstruction and the order in which that occurs differs between models (Xiao *et al.* 2021), the inclusion of poorly-matched images affects the inclusion of subsequent images. Together, this likely accounts for the differences in the reconstructed surfaces shown in Figure 9.

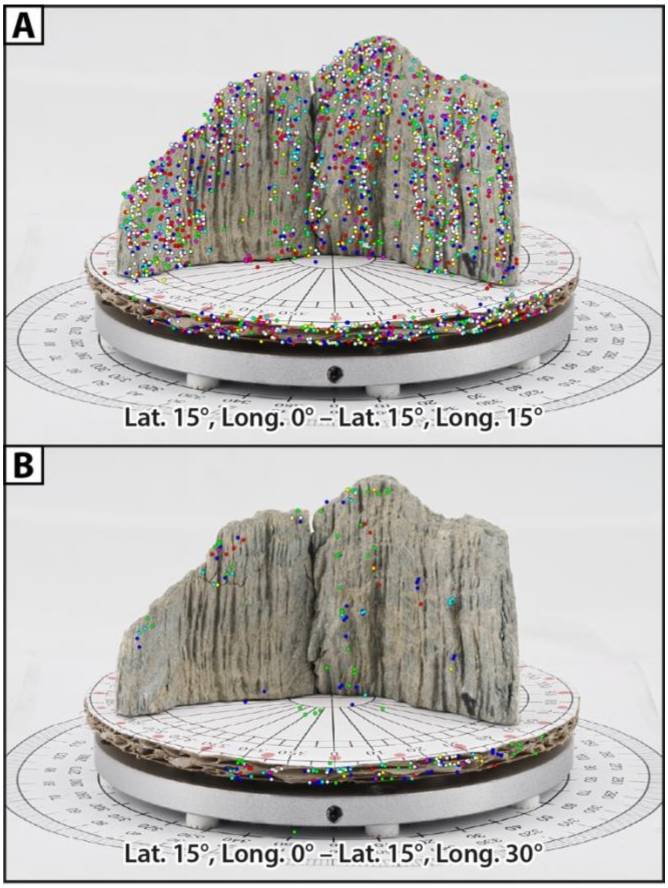

	A: Long. 0° – 15°	B: Long. 0° – 30°
Points only in image set 1	294 (21%)	17 (24%)
Points only in image set 2	191 (15%)	55 (41%)
Points only in image set 3	221 (17%)	50 (40%)
Points common to image sets 1 & 2	202 (14%, 15%)	11 (15%, 8%)
Points common to image sets 1 & 3	157 (11%, 12%)	7 (10%, 6%)
Points common to image sets 2 & 3	169 (13%, 13%)	33 (27%, 26%)
Points common to all image sets	770 (54%, 59%, 59%)	36 (51%, 27%, 29%)

Figure 21: Locations of matched keypoints for near-identical images. Red points were found in the first set of images, green points from the second, and blue points from the third. Yellow points represent matched points found in both the first and second sets of images, magenta points represent matched points found in the first and third sets of images, and cyan points represent matched points found in the second and third sets. White points represent matched points found in all three sets of images. Red numbers represent the percentages of points in the first set of images, green numbers represent the percentages of points in the second set of images, and blue numbers represent the percentages of points in the third set of images.

RAW images taken with the dedicated camera produced the most consistent results with near-identical images (Fig. 9). Practitioners are therefore cautioned that photogrammetric results may not be reproducible even under identical conditions. This is of particular relevance to studies that feature repeated photogrammetric surveys such as ground motion studies (e.g. Sun *et al.* 2024). Care should be taken in these studies to determine the margin of error in the geometry of these reconstructions to avoid erroneous interpretations.

5. Conclusion

This study demonstrates the influence of camera positioning, camera settings (ISO and image format), and camera choice on photogrammetric model quality. From these results, we can conclude actionable guidance for practitioners, especially for photogrammetry of rocks or stone materials. Despite the controlled conditions under which this study was conducted, this guidance may be directly applicable to photogrammetric surveys under 'real-world' conditions where options for lighting, camera choice, camera settings, and camera positions may be limited.

Camera networks that minimise perspective distortions between images — such as by maintaining an approximately consistent viewing direction or by including sufficient intermediate photos between extremes of viewing direction — are most likely to produce high-quality photogrammetric models. As such, camera networks containing a high diversity of viewing directions require more images to adequately capture the scene than camera networks with consistent viewing directions. Practitioners are therefore advised to choose camera placements with small and evenly-spaced changes in perspective between adjacent cameras. In the case of photogrammetric surveys using a turntable, practitioners should select short longitude intervals. For objects without overhanging regions, a single high-latitude orbit is generally sufficient to create a good quality reconstruction; however, for objects with more complex geometries, practitioners should perform multiple orbits at latitudes which allow the whole object to be seen. If multiple orbits are used, practitioners should ensure that the interval between camera positions in the latitude and longitude directions are similar so that the camera network is evenly distributed.

Digital noise in input images is observed to severely degrade photogrammetric model quality — models containing ISO 200 images performed 48% better than those containing ISO 25600 images — but noise reduction can partially mitigate this effect. As such, exposures should be balanced to keep ISO as low as possible without introducing out-of-focus or motion blur and noise reduction post-processing should be used on images observed to feature unacceptable levels of digital noise. RAW images provided a 42% improvement in model quality over JPEG images for low-noise ISO 200 images and took 41% longer to process; however, for the noisy ISO

25600 images, the in-camera noise reduction applied to the JPEG images mitigated the issues present in the RAW images. Practitioners are therefore advised to use RAW images where ISO is low and digital noise is limited if processing time is not a constraint; however, JPEG images are recommended where noise reduction is required. The smartphone was capable of producing models of near-equal quality to the Micro-Four-Thirds dedicated camera. Photogrammetric results are also demonstrated not to be reproducible, even with near-identical input images, and practitioners should be cognisant of the margin of error in their results.

This study therefore demonstrates that camera network design provides the greatest control on photogrammetric model quality and that noisy, high-ISO images also provide a significant deleterious influence on model quality. Recording format and camera choice provided only a small influence on model quality that may be weighed against other practical concerns when designing a photogrammetric survey. As such, this study provides the practitioner with the necessary quantitative comparisons to make informed choices in their survey design.

Acknowledgements

A.P. Clarke was funded by the Alexander von Humboldt Foundation.

Declaration of generative AI and AI-assisted technologies in the manuscript preparation process

During the preparation of this work the authors used Z.AI GLM-4.6 to assist in the development of scripts to rearrange data and plot elements of figures. After using this tool/service, the authors reviewed and edited the content as needed and take full responsibility for the content of the published article.

6. References

Agisoft. 2023. Agisoft Metashape Pro. Version 2.0.4. https://www.agisoft.com/features/professional-edition/.

Agisoft. 2025. Agisoft Metashape User Manual - Professional Edition, Version 2.2. Accessed: 22/11/2025. https://www.agisoft.com/pdf/metashape-pro_2_2_en.pdf.

Akçay, Ö., Erenoğlu, R.C. and Avşar, E.Ö. 2017. The Effect of Jpeg Compression in Close Range Photogrammetry. *International Journal of Engineering and Geosciences*, **2**, 35–40, https://doi.org/10.26833/ijeg.287308.

Alfio, V.S., Costantino, D. and Pepe, M. 2020. Influence of Image TIFF Format and JPEG Compression Level in the Accuracy of the 3D Model and Quality of the Orthophoto in UAV Photogrammetry. *Journal of Imaging*, **6**, 30, https://doi.org/10.3390/jimaging6050030.

Barba, S., Barbarella, M., Di Benedetto, A., Fiani, M., Gujski, L. and Limongiello, M. 2019. Accuracy Assessment of 3D Photogrammetric Models from an Unmanned Aerial Vehicle. *Drones*, **3**, 79, https://doi.org/10.3390/drones3040079.

Bartoš, K., Pukanská, K., Kseňak, Ľ., Gašinec, J. and Bella, P. 2023. Cross-Polarized SfM Photogrammetry for the Spatial Reconstruction of Challenging Surfaces, the Case Study of Dobšiná Ice Cave (Slovakia). *Remote Sensing*, **15**, 4481, https://doi.org/10.3390/rs15184481.

Bemis, S.P., Micklethwaite, S., Turner, D., James, M.R., Akciz, S., Thiele, S.T. and Bangash, H.A. 2014. Ground-based and UAV-Based photogrammetry: A multi-scale, high-resolution mapping tool for structural geology and paleoseismology. *Journal of Structural Geology*, **69**, 163–178, https://doi.org/10.1016/j.jsg.2014.10.007.

Bilmes, A., D'Elia, L., et al. 2019. Digital outcrop modelling using "structure-from- motion" photogrammetry: Acquisition strategies, validation and interpretations to different sedimentary environments. *Journal of South American Earth Sciences*, **96**, 102325, https://doi.org/10.1016/j.jsames.2019.102325.

Bisson-Larrivée, A. and LeMoine, J.-B. 2022. Photogrammetry and the impact of camera placement and angular intervals between images on model reconstruction. *Digital Applications in Archaeology and Cultural Heritage*, **26**, e00224, https://doi.org/10.1016/j.daach.2022.e00224.

Bonato, J., Wohnrath Tognoli, F.M., Costa Nogueira, F.C., De Miranda, T.S. and Inocencio, L.C. 2022. The use of network topology to assess connectivity of deformation bands in sandstone: A quantitative approach based on digital outcrop models. *Journal of Structural Geology*, **161**, 104682, https://doi.org/10.1016/j.jsg.2022.104682.

Bryan, P.G. and Clowes, M. 1997. Surveying Stonehenge By Photogrammetry. *The Photogrammetric Record*, **15**, 739–751, https://doi.org/10.1111/0031-868X.00082.

Buckley, S.J., Howell, J.A., et al. 2022. V3Geo: a cloud-based repository for virtual 3D models in geoscience. *Geoscience Communication*, **5**, 67–82, https://doi.org/10.5194/gc-5-67-2022.

Burdziakowski, P. and Bobkowska, K. 2021. UAV Photogrammetry under Poor Lighting Conditions—Accuracy Considerations. *Sensors*, **21**, 3531, https://doi.org/10.3390/s21103531.

Cawood, A.J., Bond, C.E., Howell, J.A., Butler, R.W.H. and Totake, Y. 2017. LiDAR, UAV or compass-clinometer? Accuracy, coverage and the effects on structural models. *Journal of Structural Geology*, **98**, 67–82, https://doi.org/10.1016/j.jsg.2017.04.004.

Cawood, A.J., Corradetti, A., Granado, P. and Tavani, S. 2022. Detailed structural analysis of digital outcrops: A learning example from the Kermanshah-Qulqula radiolarite basin, Zagros Belt, Iran. *Journal of Structural Geology*, **154**, 104489, https://doi.org/10.1016/j.jsg.2021.104489.

Cazes, G., Vernant, P., Baleux, F., Giuliani, C., Jouves, J. and Brugal, J.-P. 2025. Full size cave 3D modelling using close range photogrammetry and comparison with laser scanning. *Applied Geomatics*, **17**, 733–747, https://doi.org/10.1007/s12518-025-00643-5.

Claff, W.J. 2025. Read Noise in DNs versus ISO Setting. *Photons to Photos*. https://photonstophotos.net/Charts/RN_ADU.htm.

Clini, P., Nespeca, R., Angeloni, R., D'Alessio, M. and Mandolini, M. 2023. Combining Pattern Projection and Cross Polarization to Enhance 3d Reconstruction of Featureless Reflective Surfaces. *The International Archives of the Photogrammetry, Remote Sensing and Spatial Information Sciences*, **XLVIII-M-2–2023**, 427–432, https://doi.org/10.5194/isprs-archives-XLVIII-M-2-2023-427-2023.

Cui, H., Shi, T., Zhang, J., Xu, P., Meng, Y. and Shen, S. 2021. View-graph construction framework for robust and efficient structure-from-motion. *Pattern Recognition*, **114**, 107712, https://doi.org/10.1016/j.patcog.2020.107712.

Culjak, I., Abram, D., Pribanic, T., Dzapo, H. and Cifrek, M. 2012. A brief introduction to OpenCV. *In*: 2012 Proceedings of the 35th International Convention MIPRO. 1725–1730.

Cunningham, J.A. 2021. The use of photogrammetric fossil models in palaeontology education. *Evolution: Education and Outreach*, **14**, 1, https://doi.org/10.1186/s12052-020-00140-w.

Dall'Asta, E., Thoeni, K., Santise, M., Forlani, G., Giacomini, A. and Roncella, R. 2015. Network Design and Quality Checks in Automatic Orientation of Close-Range Photogrammetric Blocks. *Sensors*, **15**, 7985–8008, https://doi.org/10.3390/s150407985.

Dawson-Haggerty, M. 2023. Trimesh. Accessed: 26/11/2025. https://github.com/mikedh/trimesh

Deliry, S.I. and Avdan, U. 2021. Accuracy of Unmanned Aerial Systems Photogrammetry and Structure from Motion in Surveying and Mapping: A Review. *Journal of the Indian Society of Remote Sensing*, **49**, 1997–2017, https://doi.org/10.1007/s12524-021-01366-x.

DJI. 2021. DJI Mavic 3 User Manual. Accessed: 22/11/2025. https://dl.djicdn.com/downloads/DJI_Mavic_3/DJI_Mavic_3_User_Manual_v1.0_en.pdf

DXOMARK. 2012. Olympus M.ZUIKO DIGITAL ED 60mm F2.8 Macro Review. *DXOMARK*. http://www.dxomark.com/Lenses/Olympus/Olympus-MZUIKO-DIGITAL-ED-60mm-F28-Macro-mounted-on-Olympus-OM-D-E-M1-Mark-II---Measurements__1136.

Elad, M., Kawar, B. and Vaksman, G. 2023. Image Denoising: The Deep Learning Revolution and Beyond—A Survey Paper. *SIAM Journal on Imaging Sciences*, **16**, 1594–1654, https://doi.org/10.1137/23M1545859.

Eltner, A., Kaiser, A., Abellan, A. and Schindewolf, M. 2017. Time lapse structure-from-motion photogrammetry for continuous geomorphic monitoring. *Earth Surface Processes and Landforms*, **42**, 2240–2253, https://doi.org/10.1002/esp.4178.

Faure, Y., Grussenmeyer, P. and Landes, T. 2025. Blurred Areas in Very Short Range Photogrammetry: A Flexible Alternative to Focus-Stacking. Case Study of a Complex-Geometry Ornament of Strasbourg's Cathedral, France. *ISPRS Annals of the Photogrammetry, Remote Sensing and Spatial Information Sciences*, **X-M-2–2025**, 89–96, https://doi.org/10.5194/isprs-annals-X-M-2-2025-89-2025.

Fawzy, H.E.-D. 2019. Study the accuracy of digital close range photogrammetry technique software as a measuring tool. *Alexandria Engineering Journal*, **58**, 171–179, https://doi.org/10.1016/j.aej.2018.04.004.

Fawzy, H.E.-D., Badawy, M. and Farhan, M. 2024. The 3D photogrammetry approach of tiny model using the rotative scanning. *World Journal of Engineering*, **21**, 1020–1028, https://doi.org/10.1108/WJE-11-2022-0457.

Fleming, Z. 2022. Using virtual outcrop models and google earth to teach structural geology concepts. *Journal of Structural Geology*, **156**, 104537, https://doi.org/10.1016/j.jsg.2022.104537.

Fraser, C.S. 1984. Network Design Considerations for Non-Topographic Photogrammetry. *Photogrammetric Engineering and Remote Sensing*, **50**, 1115–1126.

Gallo, A., Muzzupappa, M. and Bruno, F. 2014. 3D reconstruction of small sized objects from a sequence of multi-focused images. *Journal of Cultural Heritage*, **15**, 173–182, https://doi.org/10.1016/j.culher.2013.04.009.

Gargari, A.M., Ebadi, H., Esmaeili, F. and Latifzadeh, S. 2023. Dynamic 3D network design for UAV-based photogrammetry in mountainous terrain. *Environmental Earth Sciences*, **82**, 188, https://doi.org/10.1007/s12665-023-10864-9.

Garilli, E., Bruno, N., Autelitano, F., Roncella, R. and Giuliani, F. 2021. Automatic detection of stone pavement's pattern based on UAV photogrammetry. *Automation in Construction*, **122**, 103477, https://doi.org/10.1016/j.autcon.2020.103477.

Georgantas, A., Brédif, M. and Pierrot-Desseilligny, M. 2012. An accuracy assessment of automated photogrammetric techniques for 3d modeling of complex interiors. *The International Archives of the Photogrammetry, Remote Sensing and Spatial Information Sciences*, **XXXIX-B3**, 23–28, https://doi.org/10.5194/isprsarchives-XXXIX-B3-23-2012.

Google. 2025. Pixel phone hardware tech specs - Pixel Phone Help. *Google Help*. https://support.google.com/pixelphone/answer/7158570?hl=en.

Guidi, G., Shafqat Malik, U. and Micoli, L.L. 2020. Optimal Lateral Displacement in Automatic Close-Range Photogrammetry. *Sensors*, **20**, 6280, https://doi.org/10.3390/s20216280.

Hahne, C., Aggoun, A., Velisavljevic, V., Fiebig, S. and Pesch, M. 2018. Baseline and Triangulation Geometry in a Standard Plenoptic Camera. *International Journal of Computer Vision*, **126**, 21–35, https://doi.org/10.1007/s11263-017-1036-4.

Harknett, J., Whitworth, M., et al. 2022. The use of immersive virtual reality for teaching fieldwork skills in complex structural terrains. *Journal of Structural Geology*, **163**, 104681, https://doi.org/10.1016/j.jsg.2022.104681.

Harman, M. 2025. Open Camera. Accessed: 24/12/2025. https://opencamera.org.uk/.

Healey, G.E. and Kondepudy, R. 1994. Radiometric CCD camera calibration and noise estimation. *IEEE Transactions on Pattern Analysis and Machine Intelligence*, **16**, 267–276, https://doi.org/10.1109/34.276126.

HeliconSoft. 2023. Helicon Focus Pro. https://www.heliconsoft.com/heliconsoft-products/helicon-focus/.

Historic England. 2017. *Photogrammetric Applications for Cultural Heritage: Guidance for Good Practice*. ISBN: 978-1-84802-502-8.

Hodač, J., Kovářová, K., Cihla, M., Matoušková, E. and Frommeltová, E. 2023. Photogrammetric Documentation of Stone Surface Topography Changes as a Tool in Conservation Praxis. *Buildings*, **13**, 439, https://doi.org/10.3390/buildings13020439.

Hottier, P. 1976. Accuracy of Close-Range Analytical Restitutions: Practical Experiments and Prediction. *Photogrammetric Engineering and Remote Sensing*, **42**, 345–375.

Howell, J., Chmielewska, M., Lewis, C., Buckley, S., Naumann, N. and Pugsley, J. 2021. *Acquisition of Data for Building Photogrammetric Virtual Outcrop Models for the Geosciences Using Remotely Piloted Vehicles (RPVs)*. preprint, https://doi.org/10.31223/X54914.

Huang, Q., Guo, X., Wang, Y., Sun, H. and Yang, L. 2024. A survey of feature matching methods. *IET Image Processing*, **18**, 1385–1410, https://doi.org/10.1049/ipr2.13032.

James, M.R., Robson, S., d'Oleire-Oltmanns, S. and Niethammer, U. 2017. Optimising UAV topographic surveys processed with structure-from-motion: Ground control quality, quantity and bundle adjustment. *Geomorphology*, **280**, 51–66, https://doi.org/10.1016/j.geomorph.2016.11.021.

Kanun, E., Alptekin, A. and Yakar, M. 2021. Cultural heritage modelling using UAV photogrammetric methods: a case study of Kanlıdivane archeological site. **1**, 24–33.

Karami, A., Battisti, R., Menna, F. and Remondino, F. 2022. 3d Digitization of Transparent and Glass Surfaces: State of the Art and Analysis of Some Methods. *The International Archives of the Photogrammetry, Remote Sensing and Spatial Information Sciences*, **XLIII-B2-2022**, 695–702, https://doi.org/10.5194/isprs-archives-XLIII-B2-2022-695-2022.

Kontogianni, G., Chliverou, R., Koutsoudis, A., Pavlidis, G. and Georgopoulos, A. 2017. Enhancing Close-up Image Based 3d Digitisation with Focus Stacking. *The International Archives of the Photogrammetry, Remote Sensing and Spatial Information Sciences*, **XLII-2/W5**, 421–425, https://doi.org/10.5194/isprs-archives-XLII-2-W5-421-2017.

Lallensack, J., Buchwitz, M. and Romilio, A. 2022. Photogrammetry in ichnology: 3D model generation, visualisation, and data extraction, https://doi.org/10.31223/X5J30D.

Li, J., Hu, Q., Ai, M. and Zhong, R. 2017. Robust feature matching via support-line voting and affine-invariant ratios. *ISPRS Journal of Photogrammetry and Remote Sensing*, **132**, 61–76, https://doi.org/10.1016/j.isprsjprs.2017.08.009.

Li, Q., Huang, H., Yu, W. and Jiang, S. 2023. Optimized Views Photogrammetry: Precision Analysis and a Large-Scale Case Study in Qingdao. *IEEE Journal of Selected Topics in Applied Earth Observations and Remote Sensing*, **16**, 1144–1159, https://doi.org/10.1109/JSTARS.2022.3233359.

Lowe, D.G. 1999. Object recognition from local scale-invariant features. *In*: *Proceedings of the Seventh IEEE International Conference on Computer Vision* – Proceedings of the Seventh IEEE International Conference on Computer Vision. 1150–1157 vol.2., https://doi.org/10.1109/ICCV.1999.790410.

Lowe, D.G. 2004. Distinctive Image Features from Scale-Invariant Keypoints. *International Journal of Computer Vision*, **60**, 91–110, https://doi.org/10.1023/B:VISI.0000029664.99615.94.

Luhmann, T., Robson, S., Kyle, S. and Boehm, J. 2023. *Close-Range Photogrammetry and 3D Imaging*, 4th Edition., https://doi.org/10.1515/9783111029672-202.

Lund Snee, J.-E., Toy, V.G. and Gessner, K. 2014. Significance of brittle deformation in the footwall of the Alpine Fault, New Zealand: Smithy Creek Fault zone. *Journal of Structural Geology*, **64**, 79–98, https://doi.org/10.1016/j.jsg.2013.06.002.

Małyszek, H.A. and Mitka, B. 2024. Impact of image file formats on the accuracy of photogrammetric models: A comparative analysis. *Geomatics, Landmanagement and Landscape*, https://doi.org/10.15576/GLL/2024.3.06.

Marín-Buzón, C., Pérez-Romero, A., López-Castro, J.L., Ben Jerbania, I. and Manzano-Agugliaro, F. 2021. Photogrammetry as a New Scientific Tool in Archaeology: Worldwide Research Trends. *Sustainability*, **13**, 5319, https://doi.org/10.3390/su13095319.

Moreno-Noguer, F. 2011. Deformation and illumination invariant feature point descriptor. *In*: *CVPR 2011* – 2011 IEEE Conference on Computer Vision and Pattern Recognition (CVPR). 1593–1600., https://doi.org/10.1109/CVPR.2011.5995529.

Nielsen, M.S., Nikolov, I., Kruse, E.K., Garnæs, J. and Madsen, C.B. 2022. Quantifying the Influence of Surface Texture and Shape on Structure from Motion 3D Reconstructions. *Sensors*, **23**, 178, https://doi.org/10.3390/s23010178.

Novikov, M., Knyaz, V. and Ravil, G. 2019. Creating digital models of paleoanthrological sample by photogrammetry and computed tomography. *In*: *Computer Science Research Notes* – WSCG’2019 - 27. International Conference in Central Europe on Computer Graphics, Visualization and Computer Vision’2019, https://doi.org/10.24132/CSRN.2019.2901.1.2.

O’Connor, J. 2018. *Impact of Image Quality on SfM Photogrammetry: Colour, Compression and Noise*. Doctoral thesis, Kingston University.

Olkowicz, M., Dabrowski, M. and Pluymakers, A. 2019. Focus stacking photogrammetry for micro-scale roughness reconstruction: a methodological study. *The Photogrammetric Record*, **34**, 11–35, https://doi.org/10.1111/phor.12270.

Olson, C.F. and Abi-Rached, H. 2010. Wide-baseline stereo vision for terrain mapping. *Machine Vision and Applications*, **21**, 713–725, https://doi.org/10.1007/s00138-009-0188-9.

Olympus Corporation. 2019. E-M5 Mark III Instruction Manual, Accessed: 22/11/2025, https://learnandsupport.getolympus.com/sites/default/files/media/files/2020/02/E-M5Mk3_ENU_01_FW110.pdf.

Oniga, V.-E., Breaban, A.-I. and Statescu, F. 2018. Determining the Optimum Number of Ground Control Points for Obtaining High Precision Results Based on UAS Images. *In*: *The 2nd International Electronic Conference on Remote Sensing* – International Electronic Conference on Remote Sensing. 352., https://doi.org/10.3390/ecrs-2-05165.

Pan, R. 2019. Defocus blur estimation in calibrated multi-view images for 3D archaeological documentation. *Digital Applications in Archaeology and Cultural Heritage*, **14**, e00109, https://doi.org/10.1016/j.daach.2019.e00109.

Panara, Y., Menegoni, N., Carboni, F. and Inama, R. 2022. 3D digital outcrop model-based analysis of fracture network along the seismogenic Mt. Vettore Fault System (Central Italy): the importance of inherited fractures. *Journal of Structural Geology*, **161**, 104654, https://doi.org/10.1016/j.jsg.2022.104654.

Passchier, C.W. 2001. Flanking structures. *Journal of Structural Geology*, **23**, 951–962, https://doi.org/10.1016/S0191-8141(00)00166-8.

Patonis, P. 2024. Comparative Evaluation of the Performance of a Mobile Device Camera and a Full-Frame Mirrorless Camera in Close-Range Photogrammetry Applications. *Sensors*, **24**, 4925, https://doi.org/10.3390/s24154925.

Plötz, T. and Roth, S. 2017. Benchmarking Denoising Algorithms with Real Photographs. *In*: *2017 IEEE Conference on Computer Vision and Pattern Recognition (CVPR)* – 2017 IEEE Conference on Computer Vision and Pattern Recognition (CVPR). 2750–2759., https://doi.org/10.1109/CVPR.2017.294.

Polidori, L. 2021. Words as tracers in the history of science and technology: the case of photogrammetry and remote sensing. *Geo-spatial Information Science*, **24**, 167–177, https://doi.org/10.1080/10095020.2020.1843375.

Pugsley, J.H., Howell, J.A., et al. 2022. Virtual field trips utilizing virtual outcrop: construction, delivery and implications for the future. *Geoscience Communication*, **5**, 227–249, https://doi.org/10.5194/gc-5-227-2022.

Pugsley, J.H., Howell, J.A., et al. 2024. Quantifying Virtual Field Trip Efficiency. *PFG – Journal of Photogrammetry, Remote Sensing and Geoinformation Science*, **92**, 679–690, https://doi.org/10.1007/s41064-024-00321-y.

Reulke, R. and Eckardt, A. 2013. Image quality and image resolution. *In*: *2013 Seventh International Conference on Sensing Technology (ICST)* – 2013 Seventh International Conference on Sensing Technology (ICST). 682–685., https://doi.org/10.1109/ICSensT.2013.6727740.

Roncella, R., Bruno, N., Diotri, F., Thoeni, K. and Giacomini, A. 2021. Photogrammetric Digital Surface Model Reconstruction in Extreme Low-Light Environments. *Remote Sensing*, **13**, 1261, https://doi.org/10.3390/rs13071261.

Rublee, E., Rabaud, V., Konolige, K. and Bradski, G. 2011. ORB: An efficient alternative to SIFT or SURF. *In*: *2011 International Conference on Computer Vision* – 2011 IEEE International Conference on Computer Vision (ICCV). 2564–2571., https://doi.org/10.1109/ICCV.2011.6126544.

Rutkofske, J.E., Pavlis, T.L. and Ramirez, S. 2022. Applications of modern digital mapping systems to Assist inclusion of persons with disabilities in geoscience education and research. *Journal of Structural Geology*, **161**, 104655, https://doi.org/10.1016/j.jsg.2022.104655.

Sieberth, T. 2020. Optical Blur Disturbs – the Influence of Optical-Blurred Images in Photogrammtry. *The International Archives of the Photogrammetry, Remote Sensing and Spatial Information Sciences*, **XLIII-B1-2020**, 383–388, https://doi.org/10.5194/isprs-archives-XLIII-B1-2020-383-2020.

Sieberth, T., Wackrow, R. and Chandler, J.H. 2014a. Influence of blur on feature matching and a geometric approach for photogrammetric deblurring. *The International Archives of the Photogrammetry, Remote Sensing and Spatial Information Sciences*, **XL–3**, 321–326, https://doi.org/10.5194/isprsarchives-XL-3-321-2014.

Sieberth, T., Wackrow, R. and Chandler, J.H. 2014b. Motion blur disturbs – the influence of motion-blurred images in photogrammetry. *The Photogrammetric Record*, **29**, 434–453, https://doi.org/10.1111/phor.12082.

Sieberth, T., Wackrow, R. and Chandler, J.H. 2015. UAV Image Blur – Its Influence and Ways to Correct It. *The International Archives of the Photogrammetry, Remote Sensing and Spatial Information Sciences*, **XL-1/W4**, 33–39, https://doi.org/10.5194/isprsarchives-XL-1-W4-33-2015.

Smith, N., Moehrle, N., Goesele, M. and Heidrich, W. 2018. Aerial path planning for urban scene reconstruction: a continuous optimization method and benchmark. *ACM Transactions on Graphics*, **37**, 1–15, https://doi.org/10.1145/3272127.3275010.

Sorrentino, G., Menna, F., et al. 2023. Close-range photogrammetry reveals morphometric changes on replicative ground stones Buchanan, B. (ed.). *PLOS ONE*, **18**, e0289807, https://doi.org/10.1371/journal.pone.0289807.

Sun, J., Yuan, G., Song, L. and Zhang, H. 2024. Unmanned Aerial Vehicles (UAVs) in Landslide Investigation and Monitoring: A Review. *Drones*, **8**, 30, https://doi.org/10.3390/drones8010030.

Surmen, H.K. 2023. Photogrammetry for 3D Reconstruction of Objects: Effects of Geometry, Texture and Photographing. *Image Analysis & Stereology*, **42**, 51–63, https://doi.org/10.5566/ias.2887.

Tannus, J. 2020. Optimizing and Automating Computerized Photogrammetry for 360° 3D Reconstruction. *In*: *2020 22nd Symposium on Virtual and Augmented Reality (SVR)* – 2020 22nd Symposium on Virtual and Augmented Reality (SVR). 267–271., https://doi.org/10.1109/SVR51698.2020.00048.

Tavani, S., Billi, A., et al. 2022. Smartphone assisted fieldwork: Towards the digital transition of geoscience fieldwork using LiDAR-equipped iPhones. *Earth-Science Reviews*, **227**, 103969, https://doi.org/10.1016/j.earscirev.2022.103969.

Thomann, J.A., Toy, V., Hawemann, F. and Martínez-Pérez, C. 2024. Unreal field trips? Gamification as key for unlocking the potential of virtual geological fields trips. *In*: EGU General Assembly 2024. EGU24-534., https://doi.org/10.5194/egusphere-egu24-534,%202024.

Tisse, C.-L., Guichard, F. and Cao, F. 2008. Does resolution really increase image quality? *In*: DiCarlo, J. M. and Rodricks, B. G. (eds) *Digital Photography IV*. 68170Q., https://doi.org/10.1117/12.766150.

Torres, G.F. and Kämäräinen, J.-K. 2023. Depth-Aware Image Compositing Model for Parallax Camera Motion Blur, https://doi.org/10.48550/arXiv.2303.09334.

Tóth, L. 2017. Resolution Limit of Small Image Sensors Size. *Acta Technica Corviniensis - Bulletin of Engineering*, **2**, 39–44.

Uzkeda, H., Poblet, J., Magán, M., Bulnes, M., Martín, S. and Fernández-Martínez, D. 2022. Virtual outcrop models: Digital techniques and an inventory of structural models from North-Northwest Iberia (Cantabrian Zone and Asturian Basin). *Journal of Structural Geology*, **157**, 104568, https://doi.org/10.1016/j.jsg.2022.104568.

Waldhäusl, P. and Ogleby, C. 1994a. 3 X 3 Rules for Simple Photogrammetric Documentation of Architecture. *In*: *Proceedings of the ISPRS Commission V Symposium* – Close Range Techniques and Machine Vision. 426–429.

Waldhäusl, P. and Ogleby, C. 1994b. 3-Rules for simple photogrammetric documentation of architecture. *International Archives of Photogrammetry and Remote Sensing*, **30**, 426–429.

Wang, J., Qu, Z., Kong, L., Yuan, W., Liu, E., Zhang, R. and Fu, R. 2025. Learning a Perspective-Invariant Descriptor for Remote Sensing Image Matching. *IEEE Transactions on Circuits and Systems for Video Technology*, 1–1, https://doi.org/10.1109/TCSVT.2025.3574761.

Wang, S.-H. and Jaw, J.-J. 2021. Turntable-Based and Artificial Texture Aided Photogrammetric 3d Reconstruction and Specification Measurement of Shuttlecock. *In*: The 42nd Asian Conference on Remote Sensing (ACRS2021).

Williams, R., Thompson, T., Orr, C., Birley, A. and Taylor, G. 2019. 3D Imaging as a Public Engagement Tool: Investigating an Ox Cranium Used in Target Practice at Vindolanda. *Theoretical Roman Archaeology Journal*, **2**, 2, https://doi.org/10.16995/traj.364.

Xiao, T., Yan, Q., Ma, W. and Deng, F. 2021. Progressive Structure from Motion by Iteratively Prioritizing and Refining Match Pairs. *Remote Sensing*, **13**, 2340, https://doi.org/10.3390/rs13122340.

Yiğit, A.Y., Erdoğan, A., Ulvi, A. and Kaçarlar, Z. 2025. Measurement-Based Evaluation of Photogrammetric Accuracy in Small Object Models Using Turntable and Manual Acquisition. *The Photogrammetric Record*, **40**, e70031, https://doi.org/10.1111/phor.70031.

Yu, G. and Morel, J.-M. 2011. ASIFT: An Algorithm for Fully Affine Invariant Comparison. *Image Processing On Line*, **1**, 11–38, https://doi.org/10.5201/ipol.2011.my-asift.

Yu, Q., Liang, J., Xiao, J., Lu, H. and Zheng, Z. 2018. A Novel perspective invariant feature transform for RGB-D images. *Computer Vision and Image Understanding*, **167**, 109–120, https://doi.org/10.1016/j.cviu.2017.12.001.

Zhou, Q.-Y., Park, J. and Koltun, V. 2018. Open3D: A Modern Library for 3D Data Processing, https://doi.org/10.48550/arXiv.1801.09847.

Ziegler, M. and Loew, S. 2019. *Mont Terri PF Experiment: Progressive Failure of Structurally-Controlled Overbreaks - Project Introduction and Overview of Work Program*. Technical; ReportENSI Erfahrungs- und Forschungsbericht.

7. List of Figures